Grain-size effects on the closure temperature of white mica in a crustal-scale extensional shear zone — Implications of in-situ ^{40}Ar/^{39}Ar laser-ablation of white mica for dating shearing and cooling (Tauern Window, Eastern Alps)

CrossMark

Andreas Scharf [a,b,*,1], Mark R. Handy [a], Stefan M. Schmid [a,c], Silvia Favaro [a], Masafumi Sudo [d], Ralf Schuster [e], Konrad Hammerschmidt [a]

[a] Department of Earth Sciences, Freie Universität Berlin, Malteserstrasse 74-100, 12249 Berlin, Germany
[b] Department of Earth Science, Sultan Qaboos University, P.O. Box 36, Al-Khoudh, P.C. 123 Muscat, Oman
[c] Institute of Geophysics, Eidgenössische Technische Hochschule (ETH), Sonneggstrasse 5, 8092 Zürich, Switzerland
[d] Institute of Earth and Environmental Science, Universität Potsdam, Karl-Liebknecht-Strasse 24-25, 14476 Potsdam-Golm, Germany
[e] Geologische Bundesanstalt, Neulinggasse 38, 1030 Wien, Austria

ABSTRACT

In-situ ^{40}Ar/^{39}Ar laser ablation dating of white-mica grains was performed on samples from the footwall of a crustal-scale extensional fault (Katschberg Normal Fault; KNF) that accommodated eastward orogen-parallel displacement of Alpine orogenic crust in the eastern part of the Tauern Window. This dating yields predominantly cooling ages ranging from 31 to 13 Myr, with most ages clustering between 21 and 17 Myr. Folded white micas that predate the main Katschberg foliation yield, within error, the same ages as white-mica grains that overgrow this foliation. However, the absolute ages of both generations are older at the base (20 Myr) where their grain size is larger (300–500 μm), than at the top and adjacent to the hangingwall (17 Myr) of this shear zone where grain size is smaller (<100–300 μm). This fining-upward trend of white-mica grain size within the KNF is associated with a reduction of the closure temperature from the base (~445 °C) to the top (<400 °C) and explains the counter-intuitive trend of downward-increasing age of cooling in the footwall. The new data show that rapid cooling within the KNF of the eastern Tauern Window started sometime before 21 Myr according to the ^{40}Ar/^{39}Ar white-mica cooling ages and between 25–21 Myr according to the new Rb/Sr white-mica ages, i.e., shortly after the attainment of the thermal peak in the Tauern Window at ~25 Myr ago. These new data, combined with literature data, support earlier cooling in the eastern part of then Tauern Window than in the western part by some 3–5 Myr.

© 2016 Elsevier B.V. All rights reserved.

1. Introduction

Determining the timing of cooling of deeply buried basement rocks is crucial for evaluating the age and rates of exhumation in orogens and for understanding the mechanisms of exhumation, e.g., the relative importance of tectonic unroofing and erosional denudation (e.g., Ring et al., 1999; Reiners and Brandon, 2006). In the Alps, two Oligo–Miocene thermal domes (Lepontine Dome, Tauern Window; "L" and "T" in inset of Fig. 1) overprint an early Cenozoic nappe stack whose units derive from

the accreted European lower plate of the Alpine orogen. Conventional thermochronology paired with petrological studies over the past four decades has shown that exhumation of both domes largely occurred in Miocene time (e.g., Clark and Jäger, 1969; Wagner and Reimer, 1972; Selverstone, 1988; Grasemann and Mancktelow, 1993; Fügenschuh et al., 1997; Neubauer et al., 1999; Luth and Willingshofer, 2008; Campani et al., 2010; Fox, 2012). However, recent in-situ dating reveals that cooling in the Tauern Window was heterogeneous and related to a combination of folding, extensional faulting and erosion (Scharf et al., 2013a).
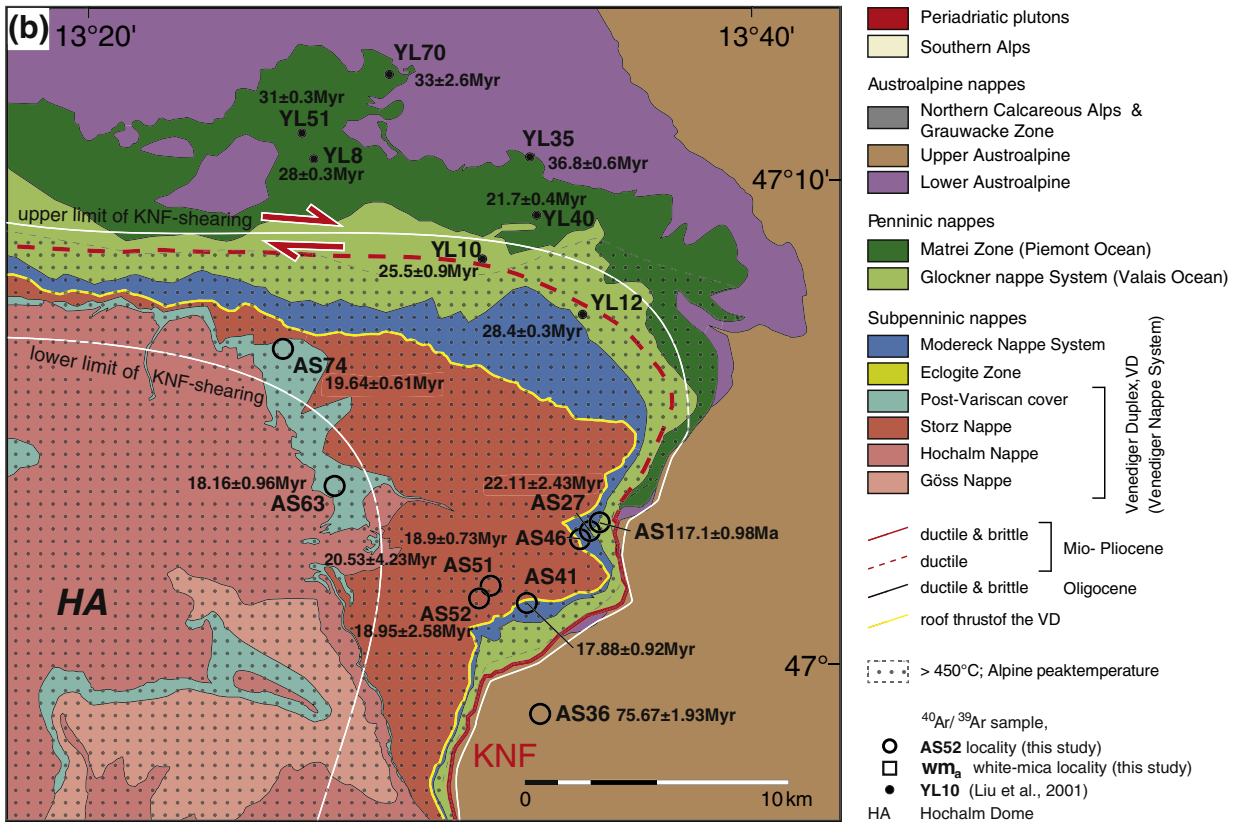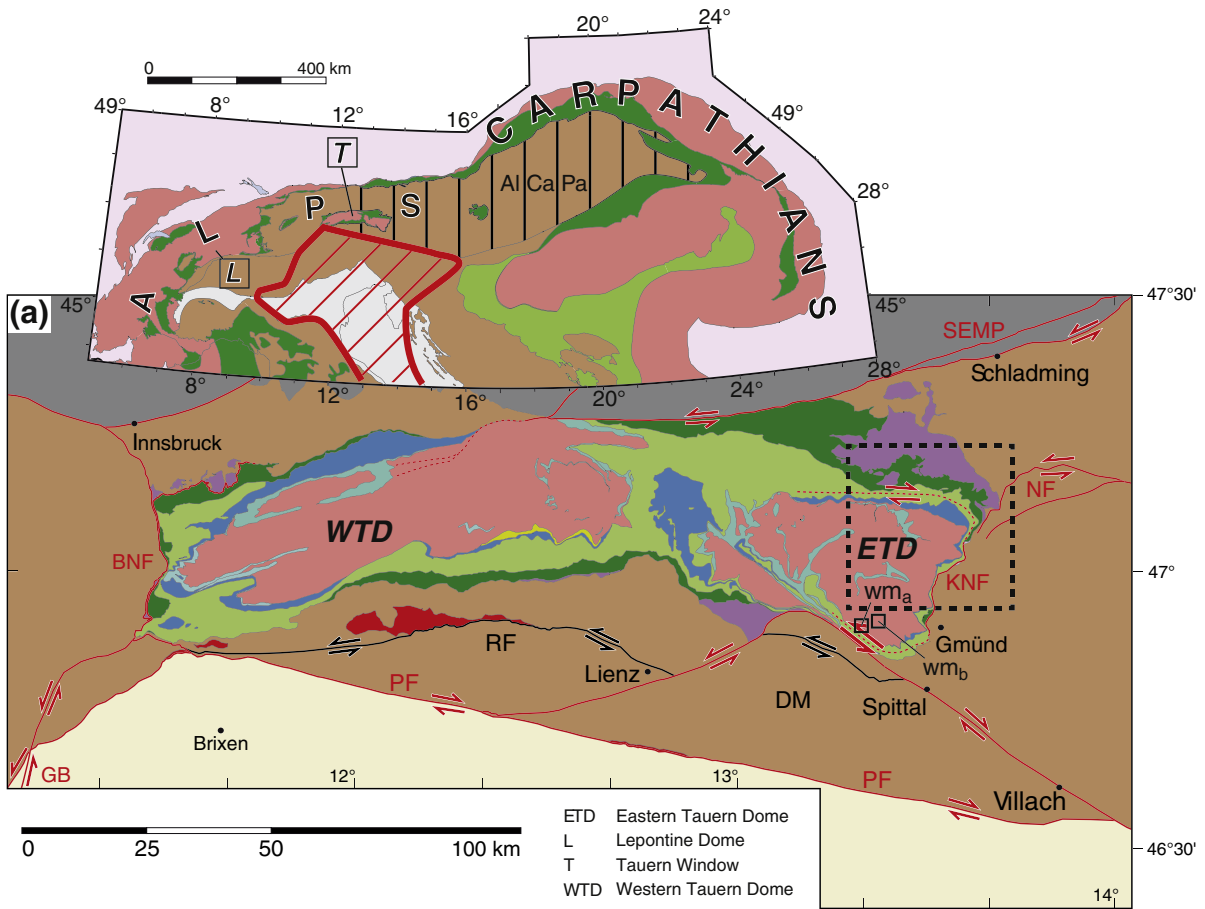
The Tauern Window comprises two main structural and metamorphic domes: the Western and Eastern Tauern domes (WTD, ETD; Fig. 1a). These expose post-nappe amphibolite-facies metamorphism in their cores and are flanked at either end by low-angle normal faults: the Brenner and Katschberg normal faults (BNF, KNF; Selverstone, 1988; Behrmann, 1988; Genser and Neubauer, 1989). Most authors relate the

(a) Legend items:

ETD Eastern Tauern Dome
L Lepontine Dome
T Tauern Window
WTD Western Tauern Dome

(b) Legend:

Periadriatic plutons
Southern Alps

Austroalpine nappes
Northern Calcareous Alps & Grauwacke Zone
Upper Austroalpine
Lower Austroalpine

Penninic nappes
Matrei Zone (Piemont Ocean)
Glockner nappe System (Valais Ocean)

Subpenninic nappes
Modereck Nappe System
Eclogite Zone
Post-Variscan cover
Storz Nappe
Hochalm Nappe
Göss Nappe

Venediger Duplex, VD (Venediger Nappe System)

ductile & brittle ⎤
ductile (dashed) ⎦ Mio- Pliocene
ductile & brittle — Oligocene
roof thrust of the VD

> 450°C; Alpine peaktemperature

$^{40}Ar/^{39}Ar$ sample,
○ AS52 locality (this study)
□ wm$_a$ white-mica locality (this study)
● YL10 (Liu et al., 2001)
HA Hochalm Dome

exhumation of the basement nappes contained in these domes to the northward indentation of that part of the Adriatic Microplate located south of the Tauern Window and east of the Giudicarie Belt (Scharf et al., 2013a and references cited therein). This late-stage deformation in front of the indenter involved a combination of broadly coeval post-nappe folding, orogen-parallel extension and erosion (e.g., Ratschbacher et al., 1991; Fügenschuh et al., 1997; Rosenberg et al., 2007; Schmid et al., 2013). However, distinguishing the relative contribution of these mechanisms has proved elusive. Compilations of the available thermochronometric data indicate that rapid exhumation (~1 mm/yr) and cooling (≤40 °C/Myr; Foeken et al., 2007) began and ended earlier in the eastern part of the Tauern Window than in the western part (e.g., Luth and Willingshofer, 2008; Scharf et al., 2013a). At first sight this is at odds with analogue models of Adriatic Microplate indentation in the Eastern Alps that predict synchronous exhumation of units in the entire Tauern Window (Ratschbacher et al., 1991; Rosenberg et al., 2007).

The amount and quality of data in the Tauern Window are not uniform. Exhumation and cooling of the western Tauern Window are fairly well constrained by thermochronometry and thermal modelling (e.g., von Blanckenburg et al., 1989; Genser et al., 1996; Fügenschuh et al., 1997). In contrast there is a relative dearth of such work in the east where past efforts (e.g., Cliff et al., 1985; Droop, 1985; Dunkl et al., 2003) have not been complemented by thermal modelling.

This paper presents new $^{40}Ar/^{39}Ar$ laser-ablation ages from white-mica aggregates and new Rb/Sr white-mica ages from the footwall of the KNF. After a brief introduction to the geological setting and methods, the in-situ age data are presented in their microstructural and metamorphic contexts. It is shown that the ages obtained do not vary with growth generation in the same sample, but with average size of the grains in the KNF. This pronounced grain-size dependence of the new $^{40}Ar/^{39}Ar$ laser-ablation ages is used to track the cooling history of the eastern Tauern Window during activity of the KNF. It is argued that cooling migrates from the base of a low-angle normal fault (445 °C) towards the top, near the hangingwall (<400 °C). This cooling trend is best explained with the smaller grain-size of the white mica and, therefore lower closure temperature towards the top of the normal fault. Finally, a comparison of the cooling histories of the eastern and western parts of the Tauern Window discusses the implications for determining whether large-scale exhumation and cooling of orogenic crust was triggered during collision or later, during indentation of the Adriatic Microplate.

2. Geological setting

2.1. Tectonic overview

The nappe stack exposed in the Tauern Window formed during convergence and collision of the Adriatic and European plates in late Cretaceous to Cenozoic times (e.g., Trümpy, 1960; Frisch, 1979; Stampfli et al., 2001; Schmid et al., 2004; Handy et al., 2010). From top to bottom, this nappe stack comprises oceanic (Penninic units: Matreier Zone and Glockner Nappe System) and Europe-derived (Subpenninic units: Modereck and Venediger nappe systems) crustal units, some of which experienced high-pressure subduction metamorphism prior to nappe stacking (Kurz et al., 2008). These units were refolded, imbricated and partly exhumed in Oligo–Miocene time before undergoing final exhumation during coeval doming and orogen-parallel

extrusion of the entire orogenic edifice towards the Pannonian Basin (e.g., Ratschbacher et al., 1991; Royden, 1993; Decker et al., 1994; Peresson and Decker, 1997; Frisch et al., 1998; Scharf et al., 2013a; Schmid et al., 2013). The Austroalpine units surrounding and overlying this nappe stack represent an earlier orogenic wedge that formed in late Cretaceous time (Eo-Alpine Orogeny Frank, 1987; Froitzheim et al., 1994, 2008; Handy et al., 2010). The base of this wedge that directly overlies the Penninic nappes shows latest Cretaceous to Cenozoic Rb/Sr and $^{40}Ar/^{39}Ar$ ages (Brewer, 1969; Hawkesworth, 1976; Liu et al., 2001) and is highly retrogressed. The ETD and WTD (Fig. 1a) expose Subpenninic basement units that experienced upper greenschist- to amphibolite-facies Barrovian-type thermal overprinting (the so-called "Tauernkristallisation"; Sander, 1911) at 30–28 Myr (Inger and Cliff, 1994; Thöni, 1999; Kurz et al., 2008). This thermal event may have lasted until 25 Myr according to new Sm/Nd ages of garnets from the WTD (Pollington and Baxter, 2010) and ETD (Favaro et al., 2015), and it overprinted a duplex system within the Europe-derived basement rocks (Venediger Duplex; Lammerer and Weger, 1998; Scharf et al., 2013a; Schmid et al., 2013).

Subsequent to this thermal overprint both Tauern domes were sheared, especially near their margins, i.e., adjacent to the overlying Austroalpine units, during final unroofing and exhumation in latest Oligocene to early Miocene time (e.g., Fügenschuh et al., 1997; Scharf et al., 2013a; Schmid et al., 2013). The Southern Alps, located south of the Periadriatic Fault and east of the Giudicarie Belt (PF and GB; Fig. 1a), were unaffected by Alpine metamorphism and represent the Adriatic Microplate Indenter in map view (Rosenberg et al., 2007). The leading edge of this indenter also included Austroalpine units north of the Periadriatic Fault and south of the Tauern Window that show little or no ductile overprint and behaved as rigid blocks during indentation (Scharf et al., 2013a).

The KNF as first described by Genser and Neubauer (1989) is a 5 to 10 km thick mylonite belt which is overprinted by cataclasites developed towards the hangingwall (Fig. 1b; see Scharf et al., 2013a and Schmid et al., 2013 for further details). The lower limit of this mylonite belt is defined by the transition from gneisses of the Venediger Nappe Complex below to a pervasive mylonitic fabric carrying a E to ESE-plunging stretching lineation within the KNF. The top of the KNF comprises 100–200 m of greenschist facies mylonite capped by cataclasites that also affect basal Austroalpine units along the eastern margin of the KNF (Fig. 1b; Scharf et al., 2013a).

2.2. Samples and their locations

Seven samples were collected from the KNF along the north-eastern margin of the Tauern Window (see Fig. 1b, Table 1 & Appendix S1 for exact locations, lithologies and tectonic units). The main foliation in these samples is oriented parallel to the macroscopic shearing plane of the KNF and is therefore assumed to have been active during orogen-parallel extensional exhumation. The protoliths of these samples comprise basement gneiss of the Venediger Nappe System and its cover, basement gneiss of the Modereck Nappe System, as well as calc-schists and metapelites of the Glockner Nappe System. Two additional samples, AS36 and AS63, are from above (hangingwall) and below (footwall) the KNF, respectively. The sample from below is a paragneiss of the post-Variscan cover from the Venediger Nappe

Fig. 1. (a) Tectonic map of the Tauern Window with investigated area (box within dotted lines). BNF — Brenner Normal Fault; DM — Drau–Möll Block; GB — Giudicarie Belt; KNF — Katschberg Normal Fault; NF — Niedere Tauern Southern Fault; PF — Periadriatic Fault; RF — Rieserferner Block; SEMP — Salzach–Ennstal–Mariazell–Puchberg Fault. Inset map shows the Lepontine Dome (L) and the Tauern Window (T) within the Alps–Carpathians Orogen with its major tectonic units derived from accreted and undeformed parts of the European continent (dark and bright red), Alpine Tethys and Neotethys (dark and light green) and accreted and autochthonous Adriatic continent (brown and light grey). The Adriatic indenter is framed by the red-striped area; AlCaPa — Alps–Carpathian–Pannonian part of accreted Adria that experienced lateral escape (vertical stripes); The sample names of the two white-mica samples wm_a and wm_b are 4R64 and 182/1/2005, respectively; (b) tectonic map of the north-eastern margin of the Tauern Window showing the location and mean age with standard deviation of the nine samples collected for $^{40}Ar/^{39}Ar$ laser ablation of white mica. Yellow line — roof thrust of the Venediger Duplex with Alpine-peak temperatures > 450 °C (Scharf et al., 2013b). White lines delimit upper and lower limits of KNF shearing. (For interpretation of the references to color in this figure legend, the reader is referred to the web version of this article.)
Maps modified from Schmid et al. (2004, 2008, 2013).

System, whereas the sample from above is a paragneiss of the Radenthein Complex belonging to the Koralpe–Wölz Nappe System of the Upper Austroalpine Unit. The ages of the white-mica grains from the seven KNF samples are expected either to date cooling to below a grain-size dependent closure temperature, or alternatively, to date white-mica formation (see review of Villa, 2010).

Table 1
Isotopic analyses for $^{40}Ar/^{39}Ar$ dating of different types of white-mica grains: Wm_1 — foliation predating the KNF; Wm_2 — main foliation of the KNF; Wm_3 — shear bands during KNF shearing; Wm_4 — grains overgrowing KNF foliation; Wm_{NO} — no preferred orientation. Note that only the smallest length of the grain dimension (divided by two = radius) was used for the closure temperature estimates as discussed in the text.

Age[Myr]	±1σ	$^{40}Ar^*/^{39}ArK$	±1σ	$^{40}Ar/^{39}Ar$	±1σ	$^{38}Ar/^{39}Ar$	±1σ	$^{37}Ar/^{39}Ar$	±1σ	$^{36}Ar/^{39}Ar$	±1σ	$\%40Ar_{atm}$	grain dimension [μm]	Microstructure
Sample AS1; J = 0.002393; metapelite; Glockner Nappe System; N 47°03'14.2" E 13°35'11.6", 1965 m															
16.54	0.83	3.888	0.194	4.727	0.037	0.012	<0.001	<0.001	<0.001	0.003	0.001	17.8	~100 x 100	Wm_1
17.06	0.47	4.011	0.110	4.463	0.011	0.013	<0.001	<0.001	<0.001	0.002	<0.001	10.1	~100 x 100	Wm_2
16.18	0.75	3.802	0.178	5.187	0.033	0.015	<0.001	<0.001	<0.001	0.005	0.001	26.7	~100 x 100	Wm_2
18.30	0.58	4.305	0.136	4.869	0.022	0.013	<0.001	<0.001	<0.001	0.002	<0.001	11.6	~100 x <100	Wm_1
17.43	0.75	4.099	0.177	4.641	0.020	0.015	<0.001	<0.001	<0.001	0.002	0.001	11.7	~100 x <100	Wm_1
16.02	0.60	3.761	0.140	5.421	0.039	0.013	<0.001	<0.001	<0.001	0.006	<0.001	30.6	~100 x <100	Wm_2
15.36	0.50	3.610	0.118	4.757	0.037	0.014	<0.001	<0.001	<0.001	0.004	<0.001	24.1	~100 x <100	Wm_2
18.06	0.30	4.248	0.068	4.592	0.030	0.012	<0.001	<0.001	<0.001	0.001	<0.001	07.1	~100 x <100	Wm_1
18.19	0.49	4.278	0.114	4.466	0.017	0.012	<0.001	<0.001	<0.001	0.001	<0.001	04.2	~100 x <100	Wm_1
17.85	0.62	4.199	0.146	4.786	0.027	0.011	<0.001	<0.001	<0.001	0.002	<0.001	12.3	~100 x <100	Wm_2
Sample AS27; J = 0.002391; metapelite; Modereck Nappe System; N 47°03'07" E 13°34'50.2", 2059 m															
22.85	1.53	5.331	0.359	9.666	0.070	0.014	<0.001	<0.001	<0.001	0.015	0.001	44.8	~1000 x 200	Wm_2
17.35	1.57	4.042	0.368	110.75	0.060	0.076	0.001	<0.001	<0.001	0.366	0.001	96.4	~1000 x 100	Wm_2
23.18	0.55	5.409	0.128	6.619	0.038	0.012	<0.001	<0.001	<0.001	0.004	<0.001	18.2	~1000 x 100	Wm_2
23.24	0.60	5.422	0.140	6.434	0.028	0.012	<0.001	<0.001	<0.001	0.003	<0.001	15.7	~1000 x 150	Wm_2
24.32	0.55	5.676	0.128	7.394	0.036	0.011	<0.001	<0.001	<0.001	0.006	<0.001	23.2	~1000 x 100	Wm_2
22.63	0.69	5.279	0.160	6.823	0.030	0.012	<0.001	<0.001	<0.001	0.005	<0.001	22.6	~1000 x 150	Wm_2
24.50	0.68	5.717	0.158	6.722	0.019	0.010	<0.001	<0.001	<0.001	0.003	<0.001	14.9	~1000 x 100	Wm_2
18.80	0.74	4.382	0.172	14.737	0.040	0.019	<0.001	<0.001	<0.001	0.036	<0.001	70.3	~1000 x 100	Wm_2
Sample AS36; J = 0.002388; paragneiss; Upper Austroalpine, Koralpe-Wölz Nappe System; N 46°59'23.8" E 13°33'20.1", 2162 m															
77.33	0.50	18.530	0.096	19.578	0.069	0.014	<0.001	<0.001	<0.001	0.004	<0.001	05.4	~1000 x 500	Wm_{NO}
77.89	0.47	18.667	0.086	19.487	0.054	0.012	<0.001	<0.001	<0.001	0.003	<0.001	04.2	~1000 x 500	Wm_{NO}
76.95	0.60	18.436	0.126	20.157	0.072	0.015	<0.001	<0.001	<0.001	0.006	<0.001	08.5	~1000 x 200	Wm_{NO}
78.68	0.49	18.860	0.093	20.190	0.044	0.013	<0.001	<0.001	<0.001	0.005	<0.001	06.6	~1000 x 500	Wm_{NO}
71.90	0.62	17.203	0.134	18.963	0.081	0.014	<0.001	<0.001	<0.001	0.006	<0.001	09.3	~1000 x 500	Wm_{NO}
74.45	0.61	17.825	0.131	18.953	0.091	0.013	<0.001	<0.001	<0.001	0.004	<0.001	06.0	~1000 x 300	Wm_{NO}
75.56	0.62	18.096	0.134	19.489	0.124	0.013	<0.001	<0.001	<0.001	0.005	<0.001	07.1	~1000 x 500	Wm_{NO}
74.41	0.66	17.793	0.144	19.271	0.093	0.012	<0.001	<0.001	<0.001	0.005	<0.001	07.7	~1000 x 500	Wm_{NO}
74.56	0.53	17.851	0.108	19.549	0.080	0.013	<0.001	<0.001	<0.001	0.006	<0.001	08.7	~1000 x 500	Wm_{NO}
75.02	0.63	17.949	0.136	18.718	0.077	0.014	<0.001	<0.001	<0.001	0.003	<0.001	04.1	~1000 x 500	Wm_{NO}
Sample AS41; J = 0.002385; metapelite; Modereck Nappe System; N 47°01'29.8" E 13°32'49.4", 2148 m															
17.61	0.48	4.148	0.114	6.025	0.023	0.013	<0.001	<0.001	<0.001	0.006	<0.001	31.2	~1000 x 100	Wm_3
19.10	0.39	4.510	0.092	4.790	0.025	0.012	<0.001	<0.001	<0.001	0.001	<0.001	05.8	~1000 x 300	Wm_2
18.14	0.48	4.281	0.114	5.220	0.023	0.015	<0.001	<0.001	<0.001	0.003	<0.001	18.0	~1000 x 200	Wm_2
17.56	0.50	4.142	0.117	5.170	0.024	0.014	<0.001	<0.001	<0.001	0.003	<0.001	19.9	~1000 x 100	Wm_2
18.73	0.27	4.421	0.063	5.079	0.024	0.013	<0.001	<0.001	<0.001	0.002	<0.001	13.0	~1000 x 200	Wm_2
15.65	0.23	3.690	0.055	4.284	0.019	0.013	<0.001	<0.001	<0.001	0.002	<0.001	13.9	~1000 x 200	Wm_2
18.06	0.44	4.261	0.104	5.125	0.030	0.014	<0.001	<0.001	<0.001	0.003	<0.001	16.9	~1000 x 100	Wm_3
17.17	0.33	4.051	0.078	4.242	0.008	0.013	<0.001	<0.001	<0.001	0.001	<0.001	04.5	~1000 x 200	Wm_2
18.31	0.31	4.321	0.073	4.949	0.026	0.014	<0.001	<0.001	<0.001	0.002	<0.001	12.7	~1000 x 200	Wm_2
18.43	0.50	4.349	0.118	4.705	0.029	0.012	<0.001	<0.001	<0.001	0.001	<0.001	07.6	~1000 x 200	Wm_2
Sample AS46; J = 0.002383; metapelite; Modereck Nappe System; N 47°02'55.1" E 13°34'44.2", 2018 m															
17.69	0.49	4.177	0.116	4.924	0.011	0.013	<0.001	<0.001	<0.001	0.003	<0.001	15.2	~1000 x 100	Wm_2
18.73	0.74	4.424	0.175	5.110	0.045	0.014	<0.001	<0.001	<0.001	0.002	0.001	13.4	~1000 x 200	Wm_2
18.89	0.30	4.463	0.072	5.462	0.040	0.012	<0.001	<0.001	<0.001	0.003	<0.001	18.3	~1000 x 100	Wm_2
19.80	0.61	4.679	0.145	5.539	0.036	0.012	<0.001	<0.001	<0.001	0.003	<0.001	15.5	~1000 x 100	Wm_2
19.55	0.46	4.618	0.109	5.003	0.029	0.013	<0.001	<0.001	<0.001	0.001	<0.001	07.7	~1000 x 200	Wm_2

Sample AS51; J = 0.00238; paragneiss; Storz Nappe; 47°01'54.1" E 13°31'45.4", 1757 m

12.22	5.14	2.883	1.213	8.696	0.440	0.018	<0.001	<0.001	<0.001	0.020	0.004	66.9	~1000 x 400	Wm_2
21.46	1.66	5.081	0.393	11.331	0.204	0.013	<0.001	<0.001	<0.001	0.021	0.001	55.2	~1000 x 300	Wm_2
14.51	2.13	3.428	0.503	8.675	0.221	0.017	<0.001	<0.001	<0.001	0.018	0.002	60.5	~1000 x 500	Wm_2
21.25	2.06	5.031	0.488	9.613	0.308	0.017	<0.001	<0.001	<0.001	0.016	0.001	47.7	~1000 x 500	Wm_2
18.62	1.52	4.396	0.359	14.017	0.221	0.015	<0.001	<0.001	<0.001	0.033	0.001	68.6	~1000 x 300	Wm_2
24.31	2.95	5.760	0.700	10.862	0.218	0.012	<0.001	<0.001	<0.001	0.017	0.002	47.0	~1000 x 300	Wm_2
19.84	0.28	4.695	0.065	5.707	0.016	0.012	<0.001	<0.001	<0.001	0.003	<0.001	17.7	~1000 x 300	Wm_2
21.17	0.75	5.012	0.178	7.350	0.033	0.014	<0.001	<0.001	<0.001	0.008	0.001	31.8	~1000 x 300	Wm_2
19.63	0.41	4.640	0.097	7.265	0.050	0.016	<0.001	<0.001	<0.001	0.009	<0.001	36.1	~1000 x 500	Wm_2
21.70	1.57	5.136	0.373	11.185	0.091	0.018	<0.001	<0.001	<0.001	0.020	0.001	54.1	~1000 x 300	Wm_2
22.66	1.22	5.367	0.290	10.641	0.092	0.017	<0.001	<0.001	<0.001	0.018	0.001	49.6	~1000 x 300	Wm_3
19.28	0.63	4.515	0.148	6.424	0.044	0.011	<0.001	<0.001	<0.001	0.006	<0.001	29.7	~1000 x 300	Wm_3
30.44	2.95	7.223	0.701	16.115	0.198	0.012	<0.001	<0.001	<0.001	0.030	0.002	55.2	~1000 x 300	Wm_2

Sample AS52; J = 0.002377; paragneiss; Storz Nappe; N 47°01'47.9" E 13°31'35.3", 1815 m

16.64	1.11	3.808	0.264	8.492	0.041	0.012	<0.001	<0.001	<0.001	0.016	0.001	55.2	~1000 x 200	Wm_2
13.53	1.39	3.170	0.328	5.352	0.067	0.015	<0.001	<0.001	<0.001	0.007	0.001	40.8	~1000 x 300	Wm_2
19.57	0.58	4.578	0.137	6.417	0.032	0.012	<0.001	<0.001	<0.001	0.006	<0.001	28.7	~1000 x 200	Wm_2
21.01	0.21	4.973	0.051	5.929	0.011	0.012	<0.001	<0.001	<0.001	0.003	<0.001	16.1	~1000 x 300	Wm_2
21.70	0.82	5.092	0.195	5.457	0.022	0.013	<0.001	<0.001	<0.001	0.001	0.001	06.7	~1000 x 200	Wm_2
15.13	0.82	3.487	0.194	5.096	0.023	0.015	<0.001	<0.001	<0.001	0.005	0.001	31.6	~1000 x 200	Wm_2
19.68	0.74	4.587	0.175	5.488	0.024	0.014	<0.001	<0.001	<0.001	0.003	0.001	16.4	~1000 x 200	Wm_2
19.49	0.56	4.601	0.133	5.728	0.016	0.013	<0.001	<0.001	<0.001	0.004	<0.001	19.7	~1000 x 300	Wm_2
19.51	0.77	4.617	0.181	6.131	0.026	0.012	<0.001	<0.001	<0.001	0.005	0.001	24.7	~1000 x 300	Wm_2
21.87	0.54	5.184	0.129	6.699	0.014	0.015	<0.001	<0.001	<0.001	0.005	<0.001	22.6	~1000 x 300	Wm_2
20.33	0.98	4.782	0.232	11.247	0.049	0.018	<0.001	<0.001	<0.001	0.022	0.001	57.5	~1000 x 300	Wm_2

Sample AS63; J = 0.002374; metapelite; Permo-mesozoic cover of Hochalm Nappe; N 47° 04'04.5" E 13°27'21.7", 1905 m

17.80	0.49	4.210	0.117	4.955	0.025	0.011	<0.001	<0.001	<0.001	0.003	<0.001	15.0	~1000 x 200	Wm_{NO}
16.49	0.72	3.864	0.171	5.781	0.027	0.014	<0.001	<0.001	<0.001	0.006	0.001	33.2	~1000 x 400	Wm_{NO}
18.91	0.39	4.477	0.093	5.510	0.028	0.013	<0.001	<0.001	<0.001	0.003	<0.001	18.7	~1000 x 200	Wm_{NO}
17.81	0.45	4.207	0.106	5.063	0.011	0.013	<0.001	<0.001	<0.001	0.003	<0.001	16.9	~1000 x 300	Wm_{NO}
18.64	0.76	4.418	0.180	4.817	0.016	0.013	<0.001	<0.001	<0.001	0.001	0.001	08.3	~1000 x 300	Wm_{NO}
17.06	0.55	4.040	0.130	4.695	0.020	0.012	<0.001	<0.001	<0.001	0.002	<0.001	13.9	~1000 x 300	Wm_{NO}
17.54	0.41	4.134	0.097	4.975	0.019	0.014	<0.001	<0.001	<0.001	0.003	<0.001	16.9	~1000 x 200	Wm_{NO}
19.67	0.78	4.657	0.185	6.246	0.013	0.014	<0.001	<0.001	<0.001	0.005	0.001	25.4	~1000 x 200	Wm_{NO}
18.27	0.22	4.319	0.052	5.486	0.031	0.014	<0.001	<0.001	<0.001	0.004	<0.001	21.3	~1000 x 200	Wm_{NO}
19.37	0.47	4.578	0.113	5.096	0.014	0.016	<0.001	<0.001	<0.001	0.002	<0.001	10.2	~1000 x 300	Wm_{NO}

Sample AS74; J = 0.00237; metapelite; Permo-mesozoic cover of Hochalm Nappe; N 47°06'51.2" E 13°25'42.8", 1363 m

20.41	0.35	4.849	0.083	5.236	0.018	0.013	<0.001	<0.001	<0.001	0.001	<0.001	07.4	500 x 500	Wm_4
19.27	0.40	4.578	0.094	4.908	0.009	0.012	<0.001	<0.001	<0.001	0.001	<0.001	06.7	~1000 x 100	Wm_2
19.28	0.42	4.580	0.100	5.255	0.021	0.014	<0.001	<0.001	<0.001	0.002	<0.001	12.8	300 x 300	Wm_4
20.19	0.30	4.796	0.072	5.224	0.029	0.013	<0.001	<0.001	<0.001	0.001	<0.001	08.2	~1000 x 100	Wm_2
19.54	0.64	4.641	0.152	5.316	0.015	0.014	<0.001	<0.001	<0.001	0.002	0.001	12.7	400 x 400	Wm_4
20.56	0.40	4.886	0.096	4.984	0.017	0.012	<0.001	<0.001	<0.001	<0.001	<0.001	02.0	400 x 400	Wm_4
19.62	0.35	4.661	0.082	5.508	0.020	0.013	<0.001	<0.001	<0.001	0.003	<0.001	15.4	~1000 x 200	Wm_2
18.59	0.50	4.416	0.119	4.909	0.019	0.014	<0.001	<0.001	<0.001	0.002	<0.001	10.1	~1000 x 200	Wm_2
18.93	0.41	4.498	0.098	4.723	0.016	0.011	<0.001	<0.001	<0.001	0.001	<0.001	04.8	~1000 x 200	Wm_2
19.99	0.44	4.748	0.105	5.030	0.016	0.012	<0.001	<0.001	<0.001	0.001	<0.001	06.6	400 x 400	Wm_4

3. Methods

3.1. Sample preparation for $^{40}Ar/^{39}Ar$ and Rb/Sr dating

The $^{40}Ar/^{39}Ar$ in-situ laser ablation technique (e.g., Kelley et al., 1994) was combined with micro-structural investigations of grain aggregates and single grains to constrain the tectono-thermal history of the eastern Tauern Window. Microprobe-quality polished samples 1 mm thick and with a diameter of 7 mm were drilled from the samples oriented parallel to the stretching lineation and perpendicular to the main foliation of the KNF.

Prior to laser ablation, samples were investigated with an electron microprobe (JEOL JXA-8200 at the Freie Universität Berlin) to determine the relationship, if any, of mineral chemistry to micro-structural position. After electron microprobe analysis, carbon-coating of the sample surface was removed by polishing. The nine samples were wrapped in commercial grade Al foil, loaded into the 99.999% pure Al container, then sent for neutron activation to the *Nuclear Research and consultancy Group* (NRG) reactor in Petten, Netherlands. There, the Al container was wrapped in a 0.5 mm thick Cd foil. Irradiation with fast neutrons (neutron flux of ~1.1 × 10^{13} n cm^{-2} s) was performed for 10 h. Fish Canyon Tuff

sanidine (27.5 Myr; Uto et al., 1997; Ishizuka, 1998) was the neutron flux-monitoring mineral used for calculating J-values.

Two months later, the samples were returned and analysed at the $^{40}Ar/^{39}Ar$ laboratory of the Universität Potsdam using the same system and conditions as described in Wiederkehr et al. (2009), Schneider et al. (2013) and Halama et al. (2014). The Nd-YAG UV pulse laser (New Wave © Gantry Dual Wave laser ablation systems) with a maximal energy of 6 mJ and a wavelength of 266 nm was used for extracting Ar gas from the samples. Sample gas was cleaned with SAES © getters and cold trap (≤ -114 °C) in the ultrahigh-vacuum purification line. After 10 min of purification by the getters and the trap, the sample gas was released on-line to the noble gas mass spectrometer (Micromass © 5400). Ages and errors were calculated according to Uto et al. (1997).

A total of 87 spot measurements were made on white micas from nine samples. Each measurement involved the following procedure: (1) analysis of a blank (b_1); (2) three measurements of a sample; and (3) measurement of a second blank (b_2). In this way, the first sample was corrected by the first blank (b_1), the third sample by the second blank (b_2) and the second sample by a mean value of the two blanks ($[b_1 + b_2] / 2$). Typical blanks for 84% of all unknown analyses of this time were 0.0001 to 0.0002 Volts for ^{40}Ar which roughly corresponds to 2–4×10^{-12} cm^3 STP (standard temperature and pressure) with our typical sensitivity (2×10^{-8} cm^3/Volts). For ^{39}Ar, ^{38}Ar and ^{37}Ar, $<2 \times 10^{-7}$ Volts, thus $<4 \times 10^{-15}$ cm^3 STP, and for ^{36}Ar, $<5 \times 10^{-7}$ Volts, thus $<1 \times 10^{-15}$ cm^3 STP, respectively. Total ^{40}Ar intensities at unknown analysis ranged from 0.0004 to 0.005 Volts were mostly ~0.001 Volts. Therefore, the ratios of total intensity/blank of 5 to 10 were kept through the analyses.

The laser-beam size used was 75 μm. The length of laser ablation on the sample surface depended on the size and orientation of the grain (parallel or perpendicular to main foliation, shear bands); for one big grain, the total length of the laser ablation was 1000–1500 μm, whereas for smaller grains the laser ablation was divided into several (up to six) segments.

Mechanical preparations for Rb/Sr isotope analyses were performed at the Geological Survey of Austria in Vienna. Before starting the separation procedure weathered surfaces were removed from the sample material. Minerals were separated by standard methods of crushing, grinding, sieving and magnetic separations. Mass of samples used for dissolution were ~100 mg for whole-rock powder, ~200 mg for white mica. Chemical preparations were performed at the Geological Survey of Austria in Vienna and at the Department of Lithospheric Research at the University of Vienna following the procedure described by Sölva et al. (2005). Element concentrations were determined by isotope dilution using mixed Rb/Sr spikes. Total procedural blanks are ≤1 ng for Rb and Sr.

Isotopic measurements were made at the Department of Geological Sciences at the University of Vienna. Rb ratios were measured at a Finnigan® MAT 262, whereas Sr ratios were analyzed with a ThermoFinnigan® Triton MC-TIMS. Sr was run from Re double filaments, whereas Rb was evaporated from Ta single filaments. During measurements, the NBS987 standard yielded $^{86}Sr/^{87}Sr = 0.710253 \pm 4$ 2Sd(m) (n = 15) on the Triton TI. Errors for the $^{87}Rb/^{86}Sr$ ratios are ± 1% based on iterative sample analysis and spike recalibration. Ages were calculated using the ISOPLOT/Ex software (Ludwig, 2001, 2003) and a Rb-decay constant of 1.42×10^{11}/yr.

4. Microstructures, metamorphism and geochemistry

4.1. Microstructures

All seven samples from the KNF (sample AS1, AS27, AS41, AS46, AS51, AS52 and AS74; Fig. 1b) have matrix minerals that underwent dynamic recrystallization (white mica, quartz ± albite ± calcite ± chlorite). Samples near the top of the KNF, i.e., near the hangingwall, preserve quartz grains with arcuate and lobate grain boundaries that

are diagnostic of fast grain-boundary-migration recrystallization (parts of AS1, AS27 and AS46). Samples near the base of the KNF show late-stage static recrystallization of quartz and albite aggregates, and fast migration in quartz aggregates (parts of AS1, AS41, AS52, AS52 and AS74). The two samples from below the footwall (AS63) and above the hangingwall of the KNF (AS36) show annealed quartz (120° grain boundaries), albite and white mica (Scharf et al., 2013a).

A combination of optical microscopy and Scanning Electron Microscope (SEM) mapping allows five different types of white-mica grains to be distinguished (Figs. 2, 3 & Table 1).

(1) Folded white micas (Wm_1) occur between domains of white micas that define the main foliation (Wm_2) and are interpreted to have formed prior to or during the activity of the KNF (see central parts of Figs. 2a, 3a & Table 1). In Fig. 2a, the trace of the folded Wm_1 grains defining the S_1 foliation is indicated by the yellow line.

(2) White-mica grains (Wm_2) define the main mylonitic foliation (S_2) of the KNF, and are not folded. They are interpreted to have grown during activity of the KNF, although we cannot rule out the possibility that some of them grew prior to the KNF and were subsequently rotated into the macroscopic shearing plane of this normal fault (Figs. 2a–c, 3a–c and 3e–f & Table 1). Note that the axial planes of the folds affecting S_1 are parallel to the main foliation (S_2), suggesting that these are F_2 folds. These microstructural relations show clearly that Wm_1 and Wm_2 grains belong to different growth generations and deformation phases. Although samples AS27 and AS52 contain one domain of white mica only (Wm_2), a significant difference in individual white-mica ages can be discerned (see Section 6.3 for further discussion).

(3) Wm_3 grains are oriented parallel to, and indeed define, the shear bands associated with the main foliation (S_2) of the KNF. Near the ends of these shear bands, the Wm_3 grains bend into concordance with the main foliation (S_2). Based on these microstructural criteria (e.g., Simpson and Schmid, 1983; Lister and Snoke, 1984), the Wm_3 grains are therefore interpreted to have formed coevally with the Wm_2 grains and thus with KNF shearing (Figs. 2c, 3c & Table 1). In contrast to Wm_1 grains, the Wm_2 and Wm_3 grains formed during a single, progressive shearing event. It is very unlikely that S_1 and S_2 formed during one progressive deformational event: first, S_1 does not bend into the S_2 shearing plane as would be expected if the white-mica growth was continuous during progressive non-coaxial shearing and second, the vergence of F_2 folds is not consistent with the top-E to -SE sense of S_2 shear for the KNF.

(4) Wm_4 grains are isometric and oriented with their cleavage oblique to all structures, as seen by the sharp and large angle of discordance between the cleavage surfaces of Wm_2 and Wm_4 grains (Figs. 2b & 3b). In addition, the Wm_4 grains are not oriented parallel to any macroscopic structures, including the KNF. The Wm_4 grains are therefore interpreted to have grown post-kinematically (Wm_4; Figs. 2b, 3b & Table 1).

(5) White micas with no preferred orientation (Wm_{NO}) are found in samples from above (sample AS36) and below the KNF (sample AS63). Associated quartz microstructures are characterized by 120° grain boundaries, indicative of annealing (Figs. 2d, 3d & Table 1). The age of the Wm_{NO} grains with respect to the Wm_1 to Wm_4 grains is unknown; white micas in the hangingwall of the KNF are probably older and related to late Cretaceous post-kinematic cooling of Austroalpine nappe units (Schuster et al., 2004, 2006; Schmid et al., 2013). In contrast, the random orientation of Wm_{NO} grains in the footwall of the KNF does not indicate whether they grew before, during or even after activity of the KNF. This point is discussed below in the light of the age data.
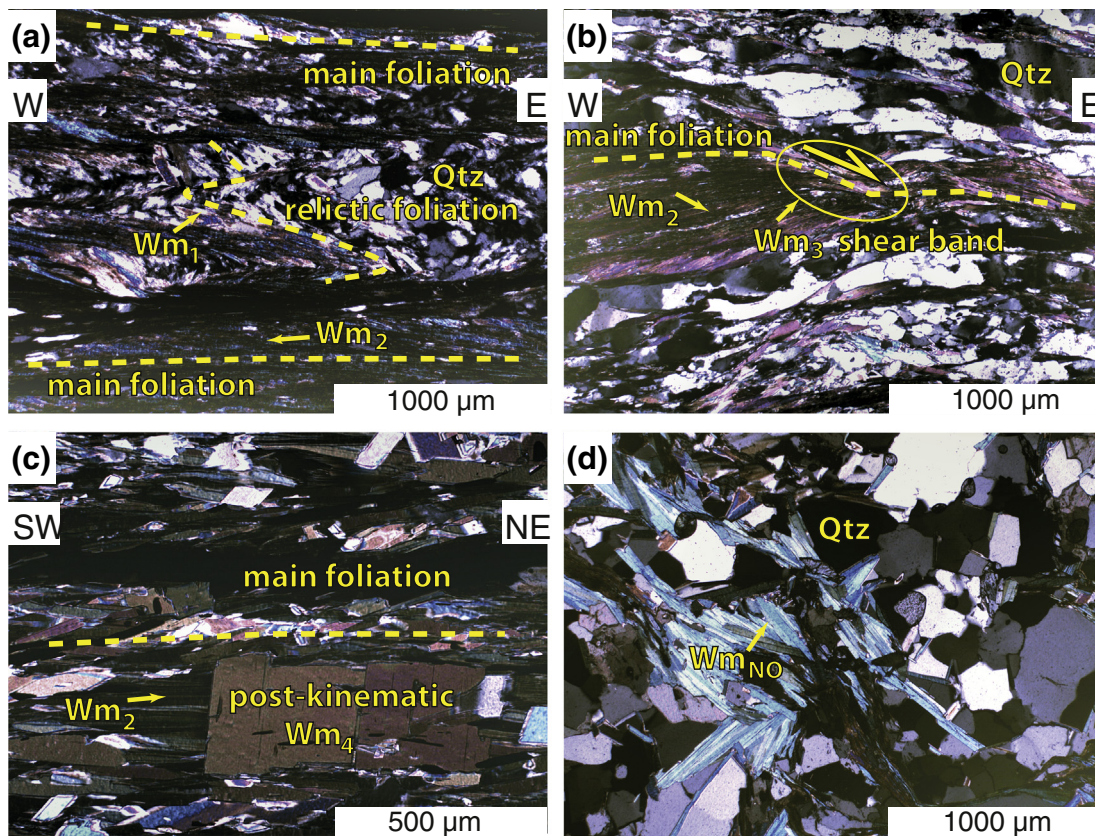
Fig. 2. Typical optical microstructures of white mica. (a) Wm_2 grains define the KNF main foliation while folded Wm_1 grains in the central part of the micrograph are relicts of an earlier schistosity (sample AS1); (b) post-kinematic Wm_4 overgrows Wm_2 defining the main KNF foliation (sample AS74); (c) Wm_3 shear bands deform Wm_2 (sample AS41); (d) Wm_{NO} lacks a preferred orientation in a fabric domain unaffected by KNF shearing (sample AS63). All photos taken with crossed nichols. (For interpretation of the references to color in this figure, the reader is referred to the web version of this article.)

4.2. Metamorphism

The Alpine peak-metamorphic temperature in the study area was inferred from Raman microspectroscopy on carbonaceous material (RSCM) and varies from ~525 °C below the footwall of the KNF to 450 °C at the top of the KNF (Scharf et al., 2013b). Thus, the peak temperature is always higher than or equal to the closure temperature of the $^{40}Ar/^{39}Ar$ white-mica system (~445–400 °C according to Harrison et al., 2009) and can vary with cooling rate and/or grain size (e.g., Dodson, 1973; Mulch et al., 2002; Harrison et al., 2009).

There is no evidence that any of the samples from the Penninic units at the eastern margin of the Tauern Window ever underwent blueschist- or eclogite-facies metamorphism. The highest pressure recorded in the Venediger Nappe System less than 10 km south of the study area (0.76 ± 0.12 GPa at ~620 °C) was reached in Oligocene time (Cliff et al., 1985; Droop, 1985; Scharf et al., 2013b). The only sample from the Upper Austroalpine unit in the hangingwall of the KNF (sample AS36; Fig. 1b) experienced late Cretaceous amphibolite-facies metamorphism and was not overprinted by Cenozoic metamorphism (Schuster et al., 2004, 2006).

4.3. Geochemistry

Microprobe analyses of the white micas at 258 single spots in all nine samples are listed in the "Appendix S1" section in Table S1. Most white micas have similar major-element compositions, irrespective of their microstructural setting (Fig. 4). Exceptions are sample AS27 (qtz-rich metapelite of the Modereck Nappe System, Al-ce: 0.32; Fe–Al-ce: 0.23 of analysis 2 in Fig. 4a) and sample AS36 (Upper Austroalpine

paragneiss, Al-ce: 0.38; Fe–Al-ce: 0.38, analysis 3 in Fig. 4a) which both have higher Al-celadonite and Fe–Al-celadonite components than the other samples of the KNF (Al-ce: 0.15–0.25; Fe–Al-ce 0.18–0.22 in Fig. 4a).

5. $^{40}Ar/^{39}Ar$ and Rb/Sr age results

White micas ranging in length from 100 to 500 µm were ablated parallel to their long axes with a UV laser. Because single grains shorter than 75 µm could not be measured, the in-situ $^{40}Ar/^{39}Ar$ ages of such small grains were estimated by ablating grain aggregates. Such aggregate ages are less reliable because it cannot be ruled out that ablation affected other interstitial minerals during gas extraction (e.g., quartz and chlorite) and/or that argon was trapped along the grain boundaries. The absolute analytical errors (1σ) of single grain ages are mostly <1 Myr, which is less than 5% relative error. Only 13 of 87 ablation measurements have an error of >1 Myr (Table 1). In the case of sample AS36, the errors are <0.7 Myr; this corresponds to an error of <1% for the absolute age (~76 Myr) in this sample.

5.1. Estimates of closure temperature

Any potential attempt to interpret the age data in terms of cooling ages rather than formation ages (discussed in Section 6) needs to take into account the fact that closure temperatures of white mica will differ amongst the samples. These expected closure temperatures were calculated using the Arrhenius parameters (E = 267.8 kJ/mol, D_o = 20 cm^2/s) of Harrison et al. (2009) and the equations of Dodson (1973). In order to apply these equations, it is necessary to make some assumptions: First, it is assumed that micas are spheres, in
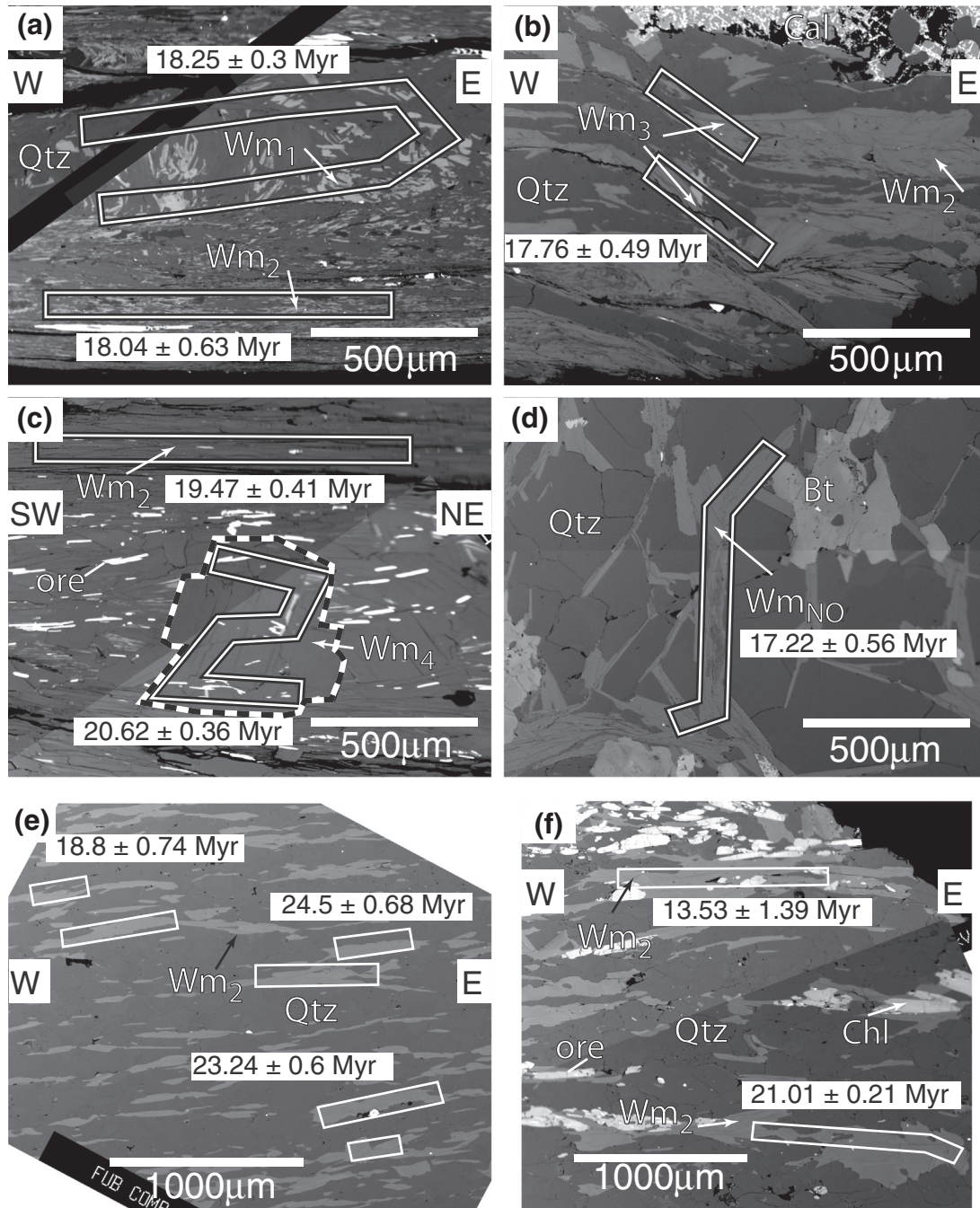
Fig. 3. Scanning electron microscope (SEM) back-scatter photomicrographs of white micas. White boxes outline laser-ablated areas with corresponding age and 1σ error. (a) Wm_2 grains along the upper and lower margins define the main foliation of the KNF, whereas folded Wm_1 grains in the centre are older mica that became reoriented during folding related to KNF shearing (sample AS1); (b) Wm_4 post-kinematic cross white mica outlined by the black/white dashed line, and main foliation (Wm_2) of the KNF (sample AS74); (c) Wm_3 grains define shear bands indicating top-E shearing within the KNF (sample AS41); (d) Wm_{NO} annealed white mica and quartz microstructures in an unfoliated sample (A63); Wm_2 defines the main foliation. Although the ages of the white mica in sample AS27 (e) and sample AS52 (f) differ significantly, no differences in the composition of the mica could be discerned. Note that in microstructural domains with grain size < 75 μm, some ages represent a composite of the ages of several white micas (e.g., samples AS1 in 'a' and AS27 in 'e').

agreement with the diffusive geometry of grains adopted by Dodson (1973). Since the white micas are generally elongate, only the half of the shortest dimension of the grains, corresponding to the radius of a sphere, was used to calculate the closure temperature. Half of the shortest dimension of the white mica grains is therefore referred to as the radius in the rest of the text and varies from <50 to ~225 μm, corresponding to a closure temperature in the range of <403 to 446 °C, respectively (Table 2). Second, a pressure of 0.5 GPa during growth of the mica is assumed. This assumed pressure of white-mica growth during exhumation in the footwall of the KNF is a very approximate value

taken to be less than the peak pressure of 0.76 ± 0.12 GPa (Droop, 1985). Third, a cooling rate of 40 °C/Myr is assumed for all rocks within and below the KNF. This cooling rate is obtained from the temperature drop of 500 to 300 °C over the 22 to 17 Myr time period constrained by the Rb/Sr white mica and biotite systems in the ETD (see Fig. 7 of Scharf et al., 2013a and references therein). A lower cooling rate of 10 °C/Myr was used for sample AS36 from the hangingwall of the KNF because cooling of these Austroalpine units from peak metamorphism at ~550 to 300 °C must have started some 100 to 75 Myr ago (Schuster and Frank, 2000).
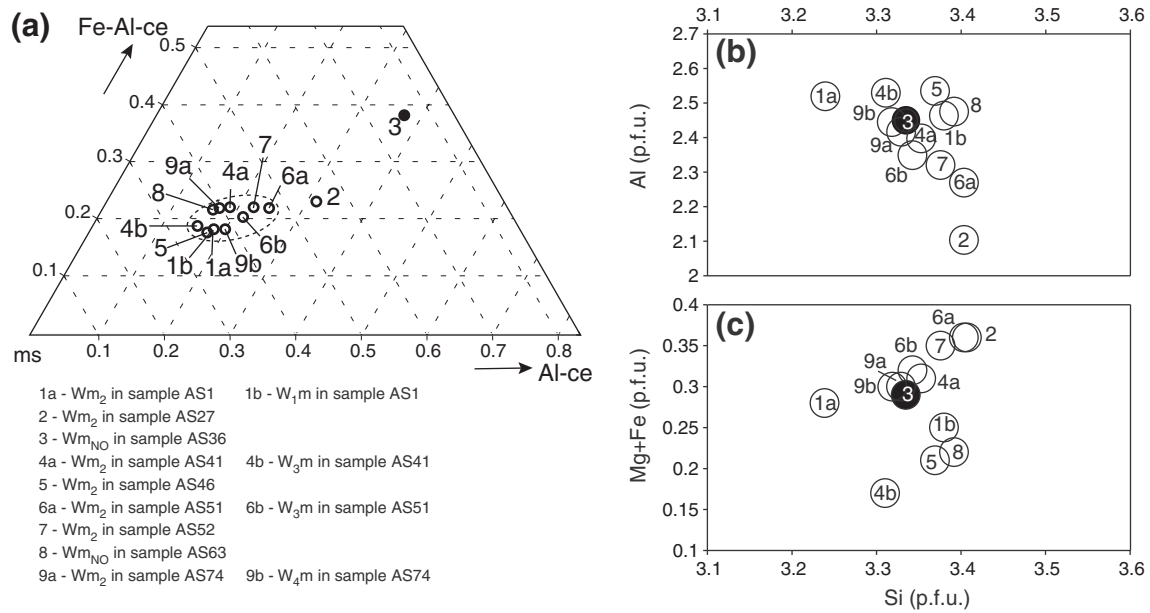
Fig. 4. Compositional range of white micas belonging to the various microstructural types measured within the nine samples analysed (Table 1). (a) Fe–Al-ce (celadonite), ms (muscovite) and Al-ce (celadonite); (b) Al (p.f.u.) versus Si (p.f.u.); (c) Fe + Mg (p.f.u.) versus Si (p.f.u.). Abbreviations: Wm_1 — refolded grains; Wm_2 — grains parallel to the main foliation; Wm_3 — white mica aligned parallel to shear bands formed during KNF shearing; Wm_4 — post-kinematic grains; Wm_{NO} — grains with no preferred orientation. The black circle refers to white mica in AS36 from the hangingwall of the KNF; open circles are white mica from within or below the KNF.

5.2. Samples from top and bottom of the KNF

Samples AS1 (Fig. 5a) and AS74 (Fig. 5h) yield remarkably similar ages despite the different types of grains that they contain. Wm_1 and Wm_2 grains from sample AS1 at the top of the KNF, e.g., near the hangingwall (Figs. 1b, 2a & 3a), scatter over a narrow range. Their average ages differ slightly but overlap within their standard deviations (17.70 ± 0.66 Myr for Wm_1 grains and 16.49 ± 0.87 Myr for Wm_2 grains; Fig. 5a & Table 1). The slightly older average ages of folded Wm_1 grains compared to the well-oriented Wm_2 grains is consistent with the microstructural evidence that Wm_1 grains are relics preserved between the Wm_2 grains defining the main foliation of the KNF (Figs. 2a

Table 2
Samples, their location with respect to the KNF, white-mica radius, estimated closure temperature based on the white-mica radius and the cooling rate (40 °C/Myr for all samples expect sample AS36 with 10 °C/Myr; see Fig. 6 and discussion in the text), and average age with standard deviation (SD). The radius is defined as the shortest dimension of the white mica divided by two. The stars at samples AS51 and AS52 indicate the apparent cooling ages without anomalous ages, as discussed in the text. AA — Austroalpine Units; GL — Glockner Nappe System; MO — Modereck Nappe System; ST — Storz Nappe; PVC — Post-Variscan cover; a — refolded Wm_1 grains; b — grains parallel to the main foliation Wm_2; c — post-kinematic Wm_4 grains. Sample locations shown in Fig. 1b.

Sample		Structural position	Radius [μm]	Closure Temperature [°C]	Age [Myr]	SD [Myr]
AS36		AA	~175[b]	419	75.67	1.93
AS1	Top	GL	10-50[a]	<403	17.70	0.66
			10-50[b]	<403	16.49	0.87
AS27		MO	~75[b]	414	22.11	2.43
AS46		MO	~75[b]	414	18.93	0.73
AS41	KNF	MO	~100[b]	422	17.88	0.92
AS51		ST	~200[b]	442	20.53	4.23
AS51✿			~175[b]	439	20.98	1.64
AS52		ST	~150[b]	434	18.95	2.58
AS52✿			~150[b]	434	20.40	0.89
AS74		PVC	~100[b]	422	19.32	0.55
	Base		~225 x ~225[c]	446	19.95	0.49
AS63		PVC	~175[b]	420	18.16	0.96

& 3a). The average age of all grains in sample AS1 is 17.10 ± 0.98 Myr. The white-mica grain radius in this sample (<50 μm) is the smallest of all samples, hence, the expected closure temperature is <403 °C.

In sample AS74 (Figs. 2b & 3b) from the base of the KNF, Wm_2 grains and post-kinematic Wm_4 grains yield slightly different average ages, although they agree within 1 sigma error (respectively, 19.32 ± 0.55 and 19.95 ± 0.49 Myr). The average age of its entire population of Wm_2 and Wm_4 grains is one of the oldest of all analysed samples (19.64 ± 0.61 Myr), even though this specimen is located at the base of the KNF where rocks are expected to have cooled later than in structurally higher positions closer to the top of the KNF. The radii of the Wm_2 (~100 μm), and Wm_4 grains (~225 μm, Tables 1 & 2) yield closure temperatures of ~420 and ~445 °C, respectively (Figs. 6 & 7).

5.3. Samples with shear bands

Two specimens (AS41 and AS51) contain Wm_2 grains defining the main KNF foliation (S_2) as well as Wm_3 grains oriented parallel to shear bands (Figs. 2c, 3c & Table 1). Hence, both white-mica generations are syn-kinematic with respect to top-E orogen-parallel extension. In sample AS41, the two measured Wm_3 grains yield ages of 18.06 ± 0.44 and 17.61 ± 0.47 Myr and are within the age range of the Wm_2 grains between 19.10 ± 0.39 and 15.65 ± 0.23 Myr. The average age of all grains in sample AS41 is 17.88 ± 0.92 Myr. The radius of white-mica grains in sample AS41 is ~100 μm, yielding a closure temperature of ~420 °C.

In sample AS51, Wm_3 grains yield ages of 22.66 ± 1.22 and 19.28 ± 0.63 Myr, whereas the Wm_2 grain ages scatter widely between 30.44 ± 2.95 to 12.22 ± 5.14 Myr (Fig. 5e & Table 1). In this sample the average age is 20.53 ± 4.23 Myr. The radius of the measured mica in specimen AS51 is ~200 μm, indicating a closure temperature of ~440 °C (Figs. 6, 7, Tables 1 & 2).

5.4. Samples with the main KNF foliation and containing only Wm_2 grains

Samples AS27, AS46 and AS52 contain only Wm_2 grains that formed during KNF shearing. Their ages vary widely (24.5–13.53 Myr) and two age subpopulations can be discerned in samples AS27 and AS52 (Fig. 5b,
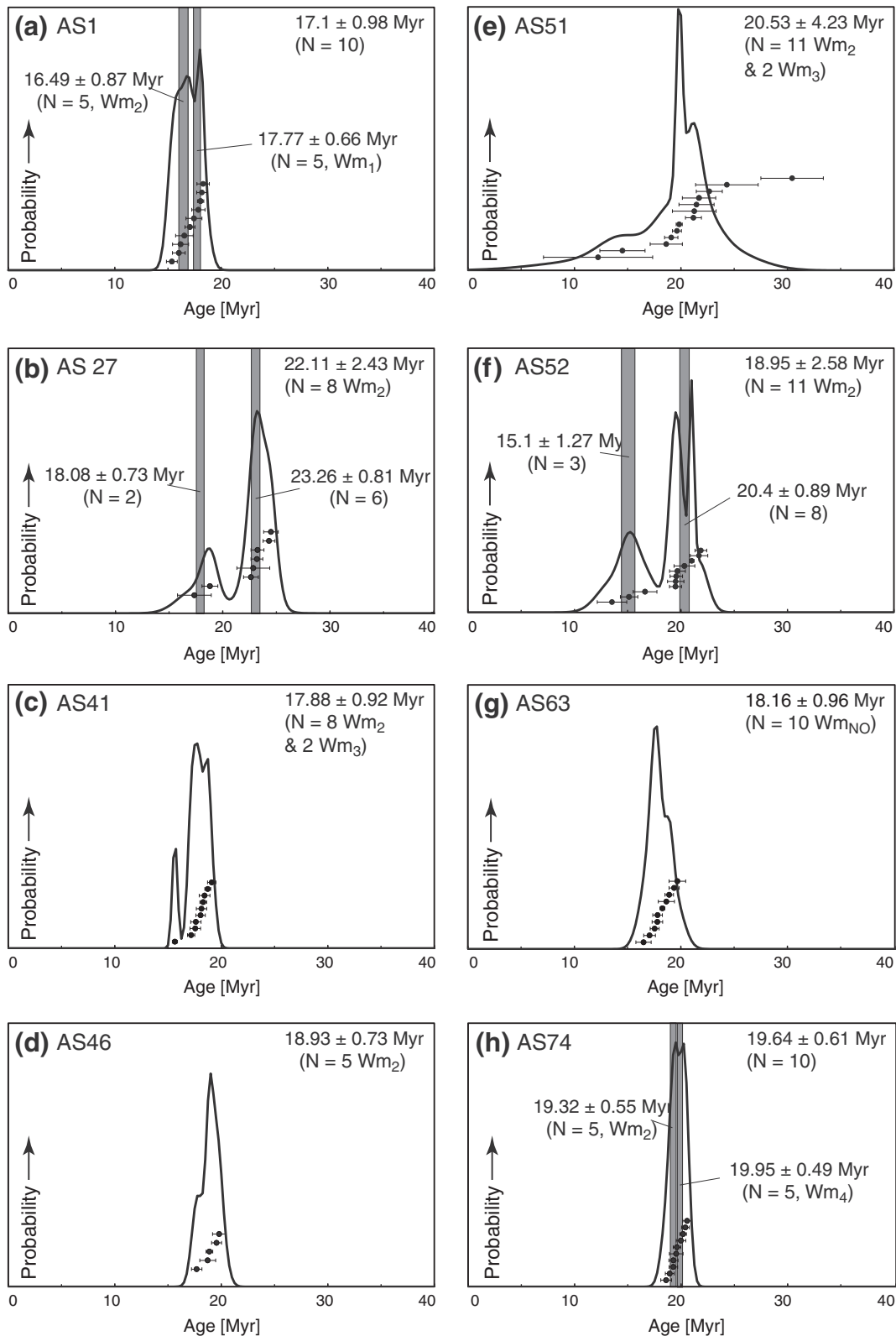
Fig. 5. Probability of grain ages of white micas versus age from the KNF and, in the case of sample AS63, from below the KNF: (a) folded Wm_1 and Wm_2 defining the KNF main foliation; (b) Wm_2 with bimodal age distribution; (c) predominantly Wm_2; (d) only Wm_2; (e) predominantly Wm_2 grains; (f) only Wm_2 grains with a bimodal age distribution; (g) post-kinematic Wm_4; (h) Wm_2 and Wm_4. Ages in upper right corner are average ages with standard deviation, N — number of grain ages used for age calculation. Black curves defining the age peaks indicate the probability of a given single grain age; black dots with 1σ error bar are the single grain data listed in Table 1; grey stripes visualize the average ages and SDs of grain sub-populations with similar average ages, Wm_1 — foliation predating the KNF; Wm_2 — main foliation of the KNF; Wm_3 — shear bands during KNF shearing; Wm_4 — grains overgrowing KNF foliation; Wm_{NO} — no preferred orientation. Note that specimens AS27 (b) and AS52 (f) preserve two distinct age populations even though only Wm_2 grains were measured. On the other hand, differences in ages obtained for different categories of white micas are negligible in samples AS1 (a) and AS74 (h).
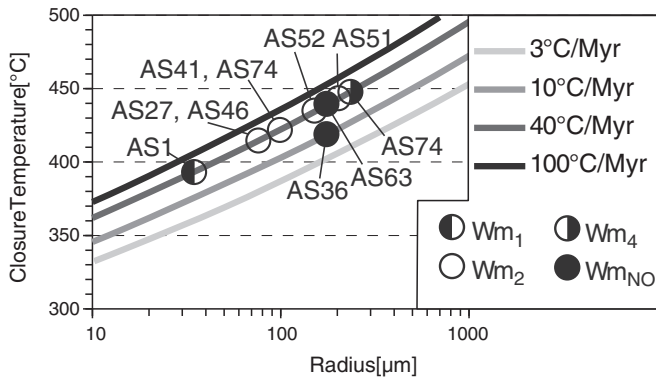
Fig. 6. Closure temperature versus radius for the white-mica grains (circles) listed in Tables 1 and 2. The radius is defined as the shortest dimension of the white mica divided by two. Lines are based on the equations of Dodson (1973) and Harrison et al. (2009) for an assumed cooling rate of 3, 10, 40 and 100 °C/Myr. Parameters used are the activation energy = 267.8 kJ/mol, the diffusional probability $D_0 = 20 \text{ cm}^2/\text{s}$ (Hames and Bowring, 1994), and are adjusted to 0.5 GPa, the diffusion geometry is spherical. Shortest grain length is treated as the radius of isometric grains or the shortest distance across elongate lath-like grains (Table 2). Sample locations are shown in Fig. 1b. Abbreviations: Wm_1 — refolded grains; Wm_2 — grains parallel to the main foliation; Wm_4 — post-kinematic grains; Wm_{NO} — grains with no preferred orientation.

f & Table 1). Sample AS27 has a bimodal age distribution with peaks at 18.08 ± 0.73 and 23.26 ± 0.81 Myr (Fig. 5b). The bimodal age distribution of sample AS52 has a younger group (three of eleven individual grains) with a mean age of 15.10 ± 1.27 Myr and an older group (eight of eleven individual grains) with a mean age of 20.40 ± 0.89 Myr (Fig. 5f). As will be discussed below, the subpopulations in both samples may reflect the anomalous white-mica chemistry (AS27), and possibly also inherited Variscan $^{40}Ar/^{39}Ar$ white mica ages (AS52). The average ages of AS27 and AS52 are 22.11 ± 2.43 and 18.95 ± 2.58 Myr, respectively. The average age of this sample is (18.90 ± 0.21 Myr; Fig. 5d & Table 1). The white-mica radii for samples AS27 and AS46 are ~75 μm and for sample AS52 the radius is ~150 μm. Hence, the calculated closure temperatures for samples AS27 and AS46 are ~415 °C, and that for sample AS52 is ~435 °C (Figs. 6, 7, Tables 1 & 2).
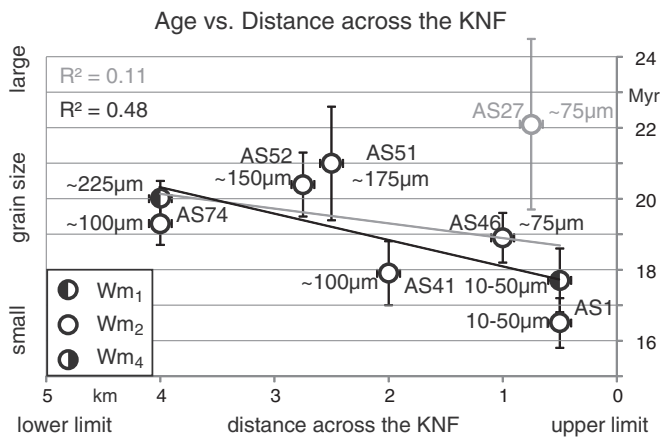
Fig. 7. Radius and age versus distance across the KNF for white-mica grains analysed in this study according to Fig. 6 and the equations of Dodson (1973) and Harrison et al. (2009). The radius is defined as the shortest dimension of the white mica divided by two. The black line shows the linear regression with the correlation coefficient (R^2). Sample AS27 was excluded for the calculation of the black regression line, since white mica of this sample consist of an anomalous composition (see Section 6.2). The regression line including sample AS27 is shown in grey. Ages and grain size radius of the white mica as listed in Table 2. Lower and upper limit marks the KNF mylonite belt (Fig. 1b). The distance across the 5 km-wide KNF mylonite belt is estimated by projecting the sample localities from map view into the cross-section 10 of Schmid et al. (2013), their Fig. 3). Wm_1 — refolded grains; Wm_2 — grains parallel to the main foliation; Wm_4 — post-kinematic grains. Sample location shown in Fig. 1b.
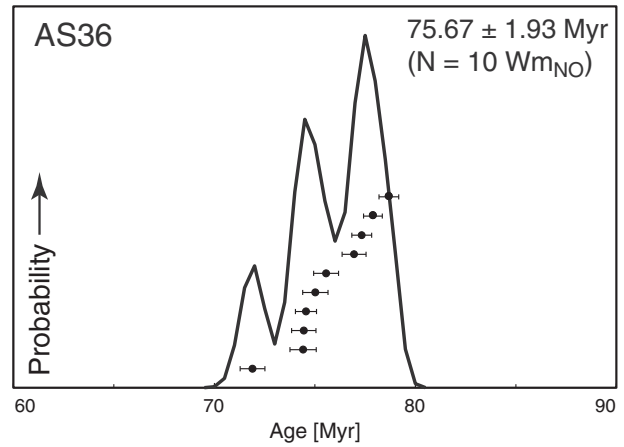

Fig. 8. Probability of grain ages of white micas versus age of sample AS36 from the Austroalpine Unit in the hangingwall of the KNF. Age in upper right corner is the average age with standard deviation, N — number of grain ages used for age calculation. Black curve indicates the probability of a given single grain age; black dots with 1σ-error bar are the single grain data listed in Table 1, Wm_{NO} — grains with no preferred orientation.

5.5. Samples from below and above the KNF

Sample AS63 is from below the lower fabric boundary of the KNF in the Venediger Nappe System (Fig. 1b), contains annealed quartz and only randomly oriented Wm_{NO} white-mica grains yielding an average age of 18.16 ± 0.96 Myr. Interestingly, this is within the age range obtained for the seven specimens collected from the KNF (Fig. 5g, Tables 1 & 2). Given the radius of these white-mica grains (~175 μm), the closure temperature is calculated to be ~440 °C (Figs. 6 & 7). Sample AS36, from the Upper Austroalpine units in the hangingwall of the KNF, has an average age of 75.67 ± 1.93 Myr (Fig. 8 & Table 1). This confirms the late Cretaceous white-mica cooling ages commonly obtained for the Upper Austroalpine units above the KNF (Brewer, 1969; Schuster and Frank, 2000). Therefore, the $^{40}Ar/^{39}Ar$ system in white mica was quite obviously not reset by Cenozoic metamorphic events in the Tauern Window. For the radius ~175 μm of these white-mica grains, the closure temperature is calculated to be ~420 °C. Note that the assumed cooling rate for this sample is slower than for the other samples (10 °C/Myr; Figs. 6, 7, Tables 1 & 2).

5.6. Summary of Ar-age results

In summary, 65% (50 out of 77) of the white-mica single grain ages measured from within and immediately below the KNF in the eastern part of the Tauern Window fall within the range of 21 to 17 Myr, irrespective of the microstructural characteristics of the individual grains. Only in the cases of paragneiss samples from the Storz Nappe (AS51 and AS52) and a metapelite from the Modereck Nappe System (AS27) does the majority of single grains ages scatter on either side of the 21–17 Myr interval (Table 1). The single sample from the hangingwall of the KNF yields late Cretaceous ages. Ages in the hangingwall that predate cooling of the footwall are indeed expected for a major low-angle normal fault, where heating of the hangingwall by the warm, exhuming footwall is usually very limited (e.g., ter Voorde and Bertotti, 1994).

5.7. Rb/Sr white-mica ages

The Rb/Sr white-mica ages are from two samples in the Hochalm and Göss nappes making up the core of the ETD, (Fig. 1b). Table 3 lists the amount of Rb and Sr, the whole-rock analysis, the $^{87}Rb/^{86}Sr$ ratio, and the errors (2σ) for these samples. The 24.4–21.1 Myr ages of the white micas in these samples are included in the discussion of the T–t

Table 3
Results for the two Rb/Sr white-mica analyses. Sample location is shown in Fig. 1a. wm — white mica; wr — whole rock.

Sample		Rock type	$^{87}Sr/^{86}Sr$	$+/-2s_m$	Rb [ppm]	Sr [ppm]	$^{87}Rb/^{86}Sr$	Age [Myr]	$+/-$
04R64	wm	Granitic	0.730748	0.000015	561.84	24.61	66.227	21.1	0.2
04R64	wr	orthogneiss	0.711393	0.000004	165.04	284.8	1.6775		
182/1/2005	wm	Bt-wm	0.850518	0.000009	825.31	7.225	335.21	24.4	0.3
182/1/2005	wr	granitic gneiss	0.737378	0.000004	238.94	83.46	8.3098		

path (Section 6.3) because the micas define the main foliation of the KNF (sample locations in Fig. 1a and further details in Favaro et al., 2015).

6. Discussion

6.1. Do the $^{40}Ar/^{39}Ar$ ages represent formational or cooling ages?

Within any given sample containing two microstructurally distinct generations of white mica, the differences in $^{40}Ar/^{39}Ar$ white-mica ages are statistically indistinguishable. For example, in sample AS1, the ages of the Wm_1 and Wm_2 grains differ by 1.28 Myr ($Wm_1 = 17.77 \pm 0.66$ Myr, $Wm_2 = 16.49 \pm 0.87$ Myr). In sample AS74, the difference is 0.63 Myr ($Wm_4 = 19.95 \pm 0.49$ Myr; $Wm_2 = 19.32 \pm 0.55$ Myr) and in samples AS41 and AS52, the Wm_3 ages fall within the range of Wm_2 ages.

There are two possible interpretations of these data: either all four types of white mica (Wm_1–Wm_4) grew within the same time span and yield formational ages, or alternatively, they all cooled below their closure temperatures at about the same time, i.e., they represent cooling ages. The second interpretation (cooling ages) is preferred for the following reasons:

(1) The microstructures described in Section 4.1 show that there were three distinct phases of white-mica growth that were kinematically unrelated to each other (Wm_1 pre-KNF, Wm_{2-3} syn-KNF and Wm_4 post-KNF). It is extremely unlikely that geometrically and kinematically unrelated white micas would grow at the same time;

(2) Sample AS74 yields slightly older $^{40}Ar/^{39}Ar$ ages for Wm_4 grains than for Wm_2 grains although they agree within 1-sigma error. This is inconsistent with the microstructural evidence that Wm_2 grains grew before Wm_4 grains. Therefore, the ages cannot possibly be formational ages. The discrepancy in the ages of Wm_2 and Wm_4 grains is best explained as due to their different grain-sizes; Wm_2 grains are smaller than Wm_4 grains and therefore have lower closure temperatures and yield correspondingly younger ages.

The fact that the maximum metamorphic temperature in the KNF and its footwall was >450–525 °C (Scharf et al., 2013b), i.e., above the expected closure temperature of 400–445 °C, lends additional support to the interpretation of these $^{40}Ar/^{39}Ar$ white-mica ages as cooling ages. This makes it unlikely that the white-mica ages are formational ages or that deformation-induced argon loss led to younger ages in some of the grains. Stated positively, the general similarity of white-mica ages within the same sample, irrespective of microstructural orientation, indicates that the ages date cooling of the samples to below the grain-size dependent closure temperatures of the $^{40}Ar/^{39}Ar$ white-mica system.

Several authors have argued that diffusion in rocks and minerals strongly depends on fluids (Villa, 2010; Warren et al., 2012; Halama et al., 2014) and that, without fluids, a much higher closure temperature should be assumed than if a fluid was present. Moreover, Warren et al. (2012) and Halama et al. (2014) confirm earlier studies showing that Ar-loss must be taken into account when interpreting $^{40}Ar/^{39}Ar$ ages

in high-pressure rocks. In our case, however, it is important to note that none of the rocks and samples in our study area contain traces of high-pressure metamorphism, nor is there any reason to suspect that they ever experienced such metamorphism; subduction-related metamorphism is restricted to other nappe units in the central part of the Tauern Window (see reviews in Schuster et al., 2004; Schmid et al., 2013 and references therein). Furthermore, fluid must have been present during shearing because the KNF mylonites contain syn-tectonically nucleated hydrous phases, including the white micas investigated here (e.g., samples AS41 & AS51). The temperature of mylonitisation, and therefore also of the fluid, was in the same range as that for intragranular Ar-diffusion in white mica (~300–500 °C). Finally, the study area contains many veins and joints filled with hydrous secondary minerals (e.g., epidote, stable at ~300–650 °C). Taken together, this indicates that excess water was present during the cooling of white mica, and therefore, that the closure temperatures for white mica were probably not any higher than assumed here.

6.2. Pattern of cooling along the KNF

In contrast to the general homogeneity of $^{40}Ar/^{39}Ar$ cooling ages within individual samples, the samples considered as a group reveal an overall trend of younger ages from the bottom to the top of the KNF (Fig. 7 & Table 2). The only exception is specimen AS27, as discussed below. This upwardly younging trend in cooling ages is opposite to the downward younging trend expected for a large normal fault (e.g., Grasemann and Mancktelow, 1993; Seward et al., 2009) where the top of the hot footwall close to the cool hangingwall would normally be thought to cool below the closure temperature earlier than the hotter, structurally lower parts of the footwall.

An explanation for this unexpected age pattern is provided by the observation that white mica tends to decrease in size from the bottom to the top of the KNF (Fig. 7, Tables 1 & 2). Specifically, white-mica grains in samples AS1, AS27 and AS46 from the top of the KNF vary in size (radius) from <50 to 100 μm, whereas in samples AS51, AS52 and AS74 from the base of the KNF, the size of white-mica grains varies from 100 to 250 μm. Smaller grains have smaller effective diffusional radii, yielding lower closure temperatures for a given cooling rate (Fig. 6; Mulch et al., 2002; Harrison et al., 2009). For white-mica grains in the KNF, the closure temperature decreased from 445 to 420 °C in initially hotter, coarser-grained samples at the base of the KNF to 420 to 400 °C in the cooler, fine-grained samples near the top.

A schematic cross-section of a generic normal fault in Fig. 9 serves to illustrate the effect of grain-size on the pattern of cooling ages in the exhumed footwall exposed at the surface today. Note that the bending of isotherms across a normal fault depends strongly on the temperature contrast between hanging- and footwalls and the exhumation rate, as well as on the thermal properties of the fault rock (e.g., thermal conductivity, density, heat capacity); generally, stronger bending reflects faster exhumation rates and/or lower rates of thermal equilibration, as modelled by Grasemann and Mancktelow (1993); Ketcham (1996), and Ehlers and Chapman (1999). However, as discussed below, the curvature of the isotherms is not the only factor influencing the age pattern in the footwall of the KNF.

An idealized normal fault with constant grain size and closure temperature across the shear zone will produce the expected pattern of progressively younger cooling ages away from the cold hangingwall because a rock from the base of the shear zone exposed at the Earth's surface today has passed through a given isotherm (marking the closure temperature) later than a rock from the top that is now also at the surface (blue exhumation paths in Fig. 9). This pattern can also result from the gradual relaxation and downward motion of isotherms after faulting has stopped.

In contrast, a normal fault like the KNF with decreasing grain size towards the cooler hangingwall will record younger ages near the top of the shear zone because a fine-grained rock exposed there at the Earth's
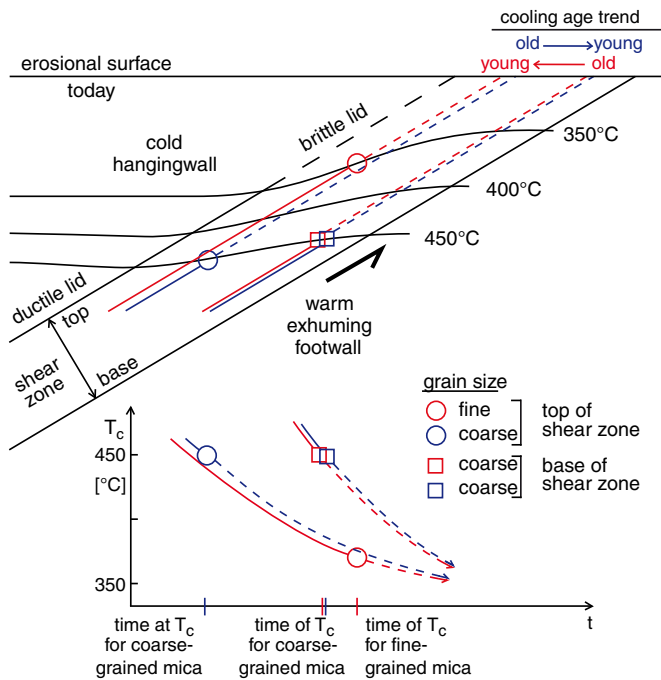
Fig. 9. Cross-section of a low-angle normal fault showing exhumation paths of rocks from the base (squares) and near the top (circles) of the shear zone. Blue paths for rock with constant white-mica grain size across and along shear zone, red paths for rock with smaller white-mica grain size near the lid than at the base of the shear zone. Grain size at base of shear zone assumed to be identical in both cases. Dashed paths indicate part of exhumation after closure of the isotopic system to diffusion. Temperature (T) versus time (t) plot shows that for a rock with constant grain size, the cooling ages young towards the base of the shear zone, whereas for rock with smaller grain size, cooling ages young towards the top because the isotherm corresponding to the lower closure temperature (T_c) is reached later (see text). Isotherms are drawn schematically based on previous thermal modeling (e.g., Grasemann and Mancktelow, 1993; Ketcham, 1996). (For interpretation of the references to color in this figure legend, the reader is referred to the web version of this article.)

surface has passed through a lower-temperature isotherm (corresponding to the reduced closure temperature) at a later time than a coarser-grained rock from the base of this shear zone (red exhumation paths in Fig. 9). Stated otherwise, the time since closure of a given isotopic system will be shorter for rocks with lower closure temperatures and therefore these systems will record younger ages than coarser grained rocks with higher closure temperatures. In the case of the KNF, the five-fold decrease in grain radii (50–225 μm) from the bottom to the top of the shear zone corresponds to a reduction in closure temperature of 50 to 100 °C (Fig. 6). In such cases, cooling ages reflect the grain-size dependence of closure temperature rather than the exhumation history of the shear zone. The contrast in white-mica grain size across shear zones is augmented if grains continue to grow at or below the base of the shear zone; this is the case below the KNF, where static grain growth (the "Tauernkristallisation" in the Venediger Nappe Complex) continued during and after the onset of KNF shearing (Scharf et al., 2013a, 2013b; Favaro et al., 2015).

Despite the strong dependence of closure temperature on grain size, cooling ages from the ^{40}Ar–^{39}Ar system in white mica are a reliable way of dating the main activity of the KNF because the closure temperatures for this system fall in the same general range (445–400 °C) as the temperatures estimated from dynamically recrystallized quartz microstructures in the KNF; the occurrence of subgrain-rotation recrystallization and fast-grain-boundary migration recrystallization (Scharf et al., 2013a) yields a temperature range of 440 to 510 ± 30 °C for geological strain rates, according to the calibration of Stipp et al. (2002).

Finally, it is important to note that the grain-size effect on the cooling-age pattern in the footwall of a normal fault is actually dependent on the relative rates of shearing (affecting the displacement and exhumation rates of the rocks) and thermal equilibration of the footwall. These factors affect the exhumation paths and the curvature of the isotherms in the shear zone. This is not shown in Fig. 9 and would require thermomechanical modelling beyond the scope of this paper. In general, higher shearing rates are expected to increase the curvature of the isotherms near the hangingwall, somewhat counteracting the grain-size effect on the age pattern discussed above and illustrated in Fig. 9.

6.3. Anomalous ages of individual white-mica grains

Some 35% of the analysed grains in the samples fall outside of the 21–17 Myr age range, and in some cases the deviations are substantial (e.g., samples AS51 and AS52). Sample AS27 with the oldest average age (22.11 ± 2.43 Myr) and an estimated closure temperature of ~415 °C (Figs. 5b, 6, 7, Tables 1 & 2) is located near the top of the KNF, close to sample AS1 which has substantially younger cooling ages (~18–16 Myr) and a lower closure temperature (<403 °C, Figs. 5a, 6, 7, Tables 1 & 2). However, Wm₂ grains in sample AS27 have slightly higher Al-ce and Fe–Al-ce components (Al-ce: 0.32; Fe–Al-ce: 0.23) than other white micas in the study area (Al-ce: 0.15–0.25; Fe–Al-ce 0.18–0.22; Section 4.3 and Fig. 4a; except sample AS36 from the hangingwall of the KNF).

Sample AS51, a paragneisses from the structurally highest Storz Nappe of the Venediger Nappe System (Fig. 1b), has an anomalously wide range of Wm₂ ages (30.44–12.22 Myr and an expected closure temperature of ~440 °C (Figs. 5e, 6, 7, Tables 1 & 2) even though all measured grains are similarly sized. This precludes a simple interpretation of this broad age distribution in terms of cooling ages. The oldest grain (30.44 ± 2.95 Myr) may preserve an isotopic signature related to the "Tauernkristallisation", which previous studies have dated in the range of 25–30 Myr (Inger and Cliff, 1994; Thöni, 1999; Liu et al., 2001; Kurz et al., 2008; Pollington and Baxter, 2010; Favaro et al., 2015). The two youngest ages from this sample have a large error (14.51 ± 2.13 Myr and 12.22 ± 5.14 Myr). Taking the upper values of their individual errors, their age would be ~17 Myr. Alternatively, these two samples may have been affected by late-stage shearing after 17 Myr ago that led to argon-loss. However, no white-mica subgrains were observed in thin section of these samples. Excluding these three anomalous ages, the average age of sample AS52 is 20.98 ± 1.64 Myr (Table 2).

Sample AS52, a paragneiss from the structurally highest Storz Nappe of the Venediger Nappe System, also has an anomalously wide, bimodal range of ages for Wm₂ grains: an older group with an average age of 20.40 ± 0.89 Myr and a younger group at 15.10 ± 1.27 Myr (Fig. 5f). Again, a simple interpretation in terms of cooling ages is not possible. The younger age group may indicate that shearing and/or fluid-influx and argon-loss lasted until ~15 Myr. However, continued shearing after 17 Myr is considered unlikely given the regional constraints on the end of shearing at ~17 Myr (see next section below and Scharf et al., 2013a).

It is interesting to note that the two samples with the broadest age distributions (AS51 and AS52) are both pre-Variscan basement rocks that experienced Variscan metamorphism and thus are likeliest to have retained old, 'excess' argon. A tentative interpretation is that these earlier events preconditioned the white micas to preserve older Argon ages in some instances, while opening them to resetting in others.

6.4. T–t paths and a comparison of new and existing Rb/Sr and $^{40}Ar/^{39}Ar$ mica ages for the Eastern Tauern Dome

Fig. 10 shows the cooling paths of the Brenner- and Katschberg normal faults (BNF, KNF), including the new $^{40}Ar/^{39}Ar$ laser-ablation data on white-mica from this study (solid red bars and brackets).
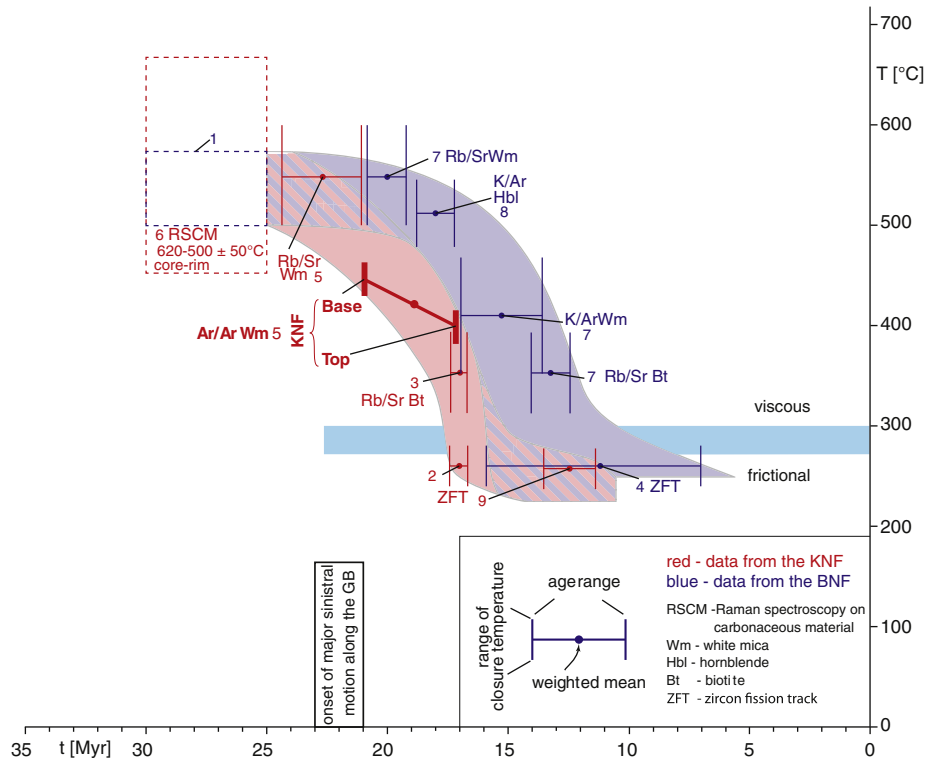
Fig. 10. Temperature-time swaths of the footwall of the Brenner and Katschberg normal faults (BNF - blue, KNF - red) including the $^{40}Ar/^{39}Ar$ data of this study for the base and top of the KNF (bold red). All samples, systems and localities are listed in the "Appendix S1" section of Scharf et al. (2013a; their Fig. 12 & Table 1). Temperature interval of frictional-viscous transition in quartz-rich rocks taken from Handy et al. (1999) and Stipp et al. (2002). Dashed boxes at upper left indicate peak temperature of the "Tauernkristallisation" (in the east after Scharf et al., 2013b; in the west after von Blanckenburg et al., 1989) at 25-30 Myr. $^{40}Ar/^{39}Ar$ single grain ages outside the 21-17 Myr age range obtained in this study are not included in this figure (see text for discussion "anomalous ages"). Closure temperatures used: Rb/Sr white mica 500 ± 50 °C (Purdy and Jäger,1976); K/Ar hornblende 530 + 33/− 40 °C (Harris, 1981); $^{40}Ar/^{39}Ar$ white mica 445-400 °C depending on grain radius and cooling rate (this study; Fig. 6); K/Ar white mica 410 °C (von Blanckenburg et al., 1989); Rb/Sr biotite 350 ± 50 °C (Jäger et al., 1967 used in von Blanckenburg et al., 1989); Zircon Fission Track 260 ± 20 °C (Foster et al., 1996 used in Fügenschuh et al., 1997; Dunkl et al., 2003; Bertrand, 2013). Note that the closure temperature assumed for the Rb/Sr white-mica system is 500 ± 50 °C, which is somewhat below the 550 ± 50 °C used by von Blanckenburg et al. (1989). Data of samples from the BNF (samples labelled 'LH' and 'PJ' in Fig. 1 of von Blanckenburg et al. (1989). The vertical bar along the time axes at 23-21 Myr indicates the probable onset of the main stage of Adriatic Microplate indentation, as discussed in the text. 1 – Selverstone et al (1984), Christensen et al. (1994), Pollington and Baxter (2010); 2 – Dunkl et al. (2013); 3 – Cliff et al. (1985); 4 – Fügenschuh et al. (1997); 5 – this study; 6 – Scharf et al. (2013b); 7 – von Blanckenburg et al. (1989); 8 – von Blanckenburg and Villa (1988); 9 – Bertrand (2013). (For interpretation of the references to color in this figure legend, the reader is referred to the web version of this article.).

As discussed above, these new data define the cooling interval of 445–400 °C, depending on grain-size, and hence record relatively early cooling of the footwall of the KNF. Both cooling trends are interpreted to reflect exhumation related to upright folding and extensional exhumation of the basement nappe complex in the footwalls of the BNF and KNF (Scharf et al., 2013a). There is a small but consistent difference of some 3 Myr in the age of cooling beneath the BNF compared to the KNF, as discussed below. The samples used to constrain the T–t paths in Fig. 10 all came from mylonites in the footwalls of the BNF and KNF (see Figs. 12 and Table 1 in Scharf et al., 2013a for locations of samples used in this compilation) and are located within about 6 km of these normal faults.

The steep part of the cooling curve for the KNF in Fig. 10 is constrained by the white mica $^{40}Ar/^{39}Ar$ single-grain data and the Rb/Sr systems in white mica and biotite, covering a wide range of closure temperatures from 550 ± 50 °C (Rb/Sr white mica; Purdy and Jäger, 1976), 445–400 °C ($^{40}Ar/^{39}Ar$ white mica; this study) and 350 ± 50 °C (Rb/Sr biotite; Jäger et al., 1967). The much larger 27–19.6 Myr range in the samples of Cliff et al. (1985) (excluding two samples with 214 ± 8 and 226 ± 8 Myr ages) from the core of the ETD is geologically ambiguous because the measured white micas are microstructurally unconstrained. In addition, Cliff et al. (1985) noticed that the Rb/Sr white-mica ages are very sensitive to uncertainties in initial isotopic composition. Their samples with the smallest analytical error (<1 Myr) cluster between 24 and 21 Myr, i.e., within the same age range of our two Rb/Sr on white-mica samples. In all samples, the closure temperature of 550 ± 50 °C for the Rb/Sr white-mica system is less than the peak temperature of

~620 °C in the core of the ETD (Droop, 1985; Scharf et al., 2013b). Two facts indicate that the Rb/Sr white-mica ages can indeed be interpreted as cooling ages: (i) the peak temperature exceeds the closure temperature of the Rb/Sr white-mica system, and (ii) that the Wm_2 grains define the main KNF foliation. Likewise, the 17.0 ± 0.3 Myr Rb/Sr biotite age of Cliff et al. (1985) from the south-eastern margin of the ETD, affected by the KNF, is interpreted as a cooling age because the closure temperature of 350 ± 50 °C for this system is much less than the peak temperature of ~500 °C in this area (Scharf et al., 2013b).

Liu et al. (2001) published $^{40}Ar/^{39}Ar$ white-mica plateau ages in the range of 37–22 Myr for samples from ophiolites and metasediments of the Penninic nappes (Glockner Nappe System, Matrei Zone) mostly located in the periphery and hangingwall of the KNF (sample locations and ages in Fig. 1b). Their ages generally decrease from outside the Tauern Window towards the KNF. The authors interpreted their ages as dating cooling after the attainment of greenschist-facies metamorphism during the stacking of the Penninic nappes in Eocene time or earlier. This suggests that cooling of the peripheral parts of the eastern Tauern Window started well before the KNF became active. Such cooling started sometime after 25–28 Myr, the age of thermal peak metamorphism, but no later than 21.1–24.1 Myr (the Rb/Sr white-mica ages). The youngest age (~22 Myr) of Liu et al. (2001) located near the KNF is interpreted to date cooling after Penninic nappe stacking in Eocene time and may mark the onset of rapid exhumation in the footwall of the KNF. Unfortunately, the white-mica ages of Liu et al. (2001) are of limited use because they are microstructurally unconstrained and represent bulk ages of all microstructural domains in one and the same sample.

To conclude, rapid cooling of rocks within and below the KNF began after the "Tauernkristallisation" which ended no earlier than 28 Myr (Inger and Cliff, 1994; Thöni, 1999; Kurz et al., 2008), probably at 25 Myr (Pollington and Baxter, 2010; Favaro et al., 2015). The cooling within the KNF started sometime before 21 Myr according to the new ^{40}Ar/^{39}Ar white-mica cooling ages in this study and sometime before 24–21 Myr according to the new Rb/Sr white mica ages. The closure temperature of ^{40}Ar/^{39}Ar white-mica in the basal part of the KNF fell below 445 °C at ~20 Myr and at the top part near the hangingwall to ~400 °C at ~17 Myr.

The Rb/Sr biotite age of Cliff et al. (1985) and zircon fission-track ages of Dunkl et al. (2003) indicate that a temperature of ~300 °C corresponding to the viscous-frictional transition in quartz-rich rocks (Handy et al., 1999; Stöckhert et al., 1999; Stipp et al., 2002) was reached at 17 Myr in the footwall of the KNF. The similar ages obtained by other geochronometers with different closure temperatures suggest that the footwall of the KNF cooled very rapidly from ~400 to 270 °C at about 17 Myr (Fig. 10). It is important to note that the ^{40}Ar/^{39}Ar white-mica cooling ages cannot significantly post-date the end of mylonitic deformation in the KNF, because peak temperatures in the rocks affected by this deformation were only ~50 °C higher than the closure temperatures of the ^{40}Ar/^{39}Ar white-mica system (Scharf et al., 2013b). Substantially younger ^{40}Ar/^{39}Ar ages of individual white-mica grains in some samples (~15 Myr) may indicate Ar-loss during shearing after 17 Myr or reduced closure temperature due to grain-size reduction. The difference of the weighted mean zircon fission-track ages of Dunkl et al. (2003; 17 Myr) and Bertrand (2013; 12.8 Myr) is attributed to the long time the rocks spent within the partial annealing zone after rapid cooling (Bertrand, 2013). As discussed in Scharf et al. (2013a), the attainment of the viscous-frictional transition along the KNF at ~17 Myr coincides with the opening of intramontane Miocene pull-apart basins in the hangingwall of the KNF (e.g., the Tamsweg and Seetal basins along the Niedere Tauern Southern Fault in Figs. 1 & 10 of Scharf et al., 2013a and discussed in their text).

6.5. Diachronous versus contemporaneous onset of rapid exhumation in the eastern and western Tauern Window

The separate T–t paths for the footwalls of the BNF and KNF in Fig. 10 indicate that the onset of rapid cooling in the eastern Tauern Window may have predated the onset in the western Tauern Window by ~2–3 Myr. Thermal modelling of cooling ages in the exhumed units beneath the BNF (Fügenschuh et al., 1997) indicates that rapid exhumation there began at ~20 Myr, some 2 Myr before the onset of rapid cooling. This fits well with biostratigraphic evidence for the onset of indentation accommodated by the Giudicarie Belt (Fig. 1a, Luciani and Silvestrini, 1996) and its lateral continuation to the west (Mt. Orfano area, Sciunnach et al. 2010) some 23 to 21 Myr ago (Fig. 10, discussion in Scharf et al., 2013a). Unfortunately, the onset of rapid exhumation in the footwall of the KNF is not constrained by thermal modelling, making a comparison of the exhumation histories of the BNF and KNF somewhat speculative. Therefore, within the limits of error for the cooling ages, the onset of rapid exhumation in the WTD and ETD may be regarded as either roughly contemporaneous at 20–21 Myr, or diachronous by some 2–3 Myr. We favor the latter interpretation in light of the consistency with which the various of isotopic systems (Fig. 10; Rb/Sr wm and bt, K–Ar hbl, ZFT) yield earlier cooling ages in the east than in the west. Even if one assumes a shorter delay time (<2 Myr) between rapid exhumation and cooling in the eastern Tauern Window, the onset of rapid exhumation in the eastern must have begun before 25–21 Myr ago, the age range of the new Rb/Sr white mica ages and the oldest ^{40}Ar/^{39}Ar white mica cooling ages in this study. This is earlier than indicated by the biostratigraphic constraints on the onset of indentation cited above (23–21 Myr). In fact, Pomella et al. (2011, 2012) set the onset of indentation of the Adriatic Microplate east of the Giudicarie Belt in late Oligocene to earliest Miocene time based on isotopic age constraints on transpression and bending of the Periadriatic Fault at its junction with the Giudicarie Fault. However, they do not specify absolute ages for this beyond the kinematic necessity that this bending related to indentation must have post-dated Paleogene dextral motion on the Periadriatic fault (Pomella et al., 2011; Fig. 11).

The possibility that exhumation and cooling of the Tauern Window was diachronous raises the question of how. Analogue models of Eastern Alpine indentation using a rigid indenter with a straight front produce upright folds and thrusts that exhume orogenic crust directly in front of the indenter; however (e.g., Ratschbacher et al., 1991; Rosenberg et al., 2007), they produce little or no orogen-parallel extensional exhumation and do not hint at possible diachronous exhumation of deeply buried orogenic crust. We suspect, however, that the indenter front was not straight, but rather comprised two blocks of semi-rigid Austro-alpine crust north of the Periadriatic Fault (marked RF and DM in Fig. 1; Scharf et al., 2013a) that individuated during N-S convergence and indented the orogenic crust (Frisch et al., 1998; Linzer et al., 2002) earlier in the eastern part of the Tauern Window than in the west (Favaro et al., 2015). A full test of this model awaits thermal modelling of cooling ages in the eastern Tauern Window, as well as analogue modelling of indentation with irregular indenter fronts.

7. Conclusions

This study shows that the majority (65%) of white-mica aggregates ages obtained by ^{40}Ar/^{39}Ar laser ablation date cooling below closure temperatures ranging from 445 to <400 °C, depending on grain size, during top-SE extensional shearing at the eastern margin of the Tauern Window. When combined with new Rb/Sr white-mica cooling ages and existing thermochronological ages, the ^{40}Ar/^{39}Ar laser ablation ages constrain rapid cooling in the Eastern Tauern Dome (ETD) to have started in the latest Oligocene–earliest Miocene, i.e., sometime between 25 and 21 Myr, and the rapid cooling have ended no later than 17 Myr. Moreover, the new ^{40}Ar/^{39}Ar white-mica ages indicate that cooling in the KNF reached 445 °C at ~20 Myr and subsequently migrated upwards within the KNF towards the already-cool Austroalpine units in the hangingwall. Near the hangingwall, where the grain-size of white mica within the KNF is smaller, temperatures reached the ~400 °C closure temperature of the ^{40}Ar/^{39}Ar white-mica system at ~17 Myr. The almost identical ages provided by Rb/Sr on biotite, zircon fission track and ^{40}Ar/^{39}Ar white-mica systems in samples from the top of the KNF indicate that this part of the shear zone cooled very rapidly from ~400 to 270 °C. The ^{40}Ar/^{39}Ar white-mica thermochronomter is well suited to date the early-stage rapid cooling history of the KNF because the interval of grain-size dependent closure temperatures (445–400 °C) overlaps with the range of temperatures obtained from dynamically recrystallized quartz microstructures (440–510° ± 30 °C; Stipp et al., 2002). A transition from viscous to cataclastic flow at the top of the KNF at ~17 Myr coincides temporally with the opening of intramontane pull-apart basins immediately east of and in the hangingwall of the KNF (Scharf et al., 2013a).

Appendix A. Supplementary data

Supplementary data to this article can be found online at http://dx.doi.org/10.1016/j.tecto.2016.02.014.

References

Behrmann, J.H., 1988. Crustal scale extension in a convergent orogen: the Sterzing–Steinach mylonite zone in the eastern Alps. Geodin. Acta 2, 63–73.

Bertrand, A., 2013. Exhuming the Core of Collisional Orogens, the Tauern Window (Eastern-Alps) A Geochronological, Modelling and Structural Study PhD thesis Freie Universität Berlin, Berlin, Germany, p. 196.

Brewer, M.S., 1969. Excess radiogenic argon in metamorphic micas from the Eastern Alps, Austria. Earth Planet. Sci. Lett. 6, 321–331.

Campani, M., Herman, F., Mancktelow, N.S., 2010. Two- and three-dimensional thermal modelling of a low-angle detachment: exhumation history of the Simplon Fault Zone, central Alps. J. Geophys. Res. 115, B10420. http://dx.doi.org/10.1029/2009JB007036.

Christensen, J.N., Selverstone, J., Rosenfeld, J.L., De Paolo, D.J., 1994. Correlation by Rb–Sr geochronology of garnet growth histories from different structural levels within the Tauern Window, Eastern Alps. Contrib. Mineral. Petrol. 118, 1–12.

Clark, S.P., Jäger, E., 1969. Denudation rate in the Alps from geochronologic and heat flow data. Am. J. Sci. 267 (10), 1143–1160.

Cliff, R.A., Droop, G.T.R., Rex, D.C., 1985. Alpine metamorphism in the south-east Tauern Window, Austria: 2. Rates of heating, cooling and uplift. J. Metamorph. Petrol. 3, 403–415.

Decker, K., Peresson, H., Faupl, P., 1994. Die miozäne Tektonik der östlichen Kalkalpen: Kinematik, Paläospannung und Deformationsaufteilung während der „lateralen Extrusion" der Zentralalpen. Jahrb. Geol. Bundesanst., Wien 137, 5–18.

Dodson, H., 1973. Closure temperature in cooling geochronological and petrological systems. Contrib. Mineral. Petrol. 40, 259–274.

Droop, G.T.R., 1985. Alpine metamorphism in the south-east Tauern Window, Austria: 1. P–T variations in space and time. J. Metamorph. Geol. 3, 371–402.

Dunkl, I., Frisch, W., Grundmann, G., 2003. Zircon fission track thermochronology of the southeastern part of the Tauern Window and adjacent Austroalpine margin, Eastern Alps. Eclogae Geol. Helv. 96, 209–217.

Ehlers, T.A., Chapman, D.S., 1999. Normal fault thermal regimes: conductive and hydro-thermal heat transfer surrounding the Wasatch fault, Utah. Tectonophysics 312, 217–234.

Favaro, S., Handy, M.R., Schuster, R., Scharf, A., Pestal, G., 2015. Transition from orogen-perpendicular to orogen-parallel exhumation and cooling during crustal indentation – key constraints from $^{147}Sm/^{144}Nd$ and $^{87}Rb/^{86}Sr$ geochronology (Tauern Window, Alps). Tectonophysics (accepted for publication).

Foeken, J.P.T., Persano, C., Stuart, F.M., ter Voorde, M., 2007. Role of topography in iso-therm perturbation: apatite (U–Th)/He and fission track results from the Malta tun-nel, Tauern Window, Austria. Tectonics 26, TC3006. http://dx.doi.org/10.1029/2006TC002049.

Foster, D.A., Gleadow, A.J.W., Noble, W.P., 1996. Sphene and zircon fission track closure temperature revisited: empirical calibration from $^{40}Ar/^{39}Ar$ diffusion studies of K-feldspar and biotite. International Workshop on Fission-Track Dating, Gent, Abstracts 37.

Fox, M., 2012. The Inversion of Low-Temperature Thermochronometry to Extract Spatial-ly and Temporally Varying Exhumation Rates Within the Alps PhD thesis ETH Zürich, Switzerland, p. 283 (No. 20851).

Frank, W., 1987. Evolution of the Austroalpine elements in the Cretaceous. In: Flügel, H.W., Faupl, P. (Eds.), Geodynamics of the Eastern Alps.Deuticke, Wien, pp. 379–406

Frisch, W., 1979. Tectonic progradation and plate tectonic evolution of the Alps. Tectonophysics 60, 121–139.

Frisch, W., Kuhlemann, J., Dunkl, I., Brügel, A., 1998. Palinspastic reconstruction and topographic evolution of the Eastern Alps during late Tertiary tectonic extrusion. Tectonophysics 297, 1–15.

Froitzheim, N., Schmid, S.M., Conti, P., 1994. Repeated change from crustal shortening to orogen-parallel extension in the Austroalpine units of Graubünden. Eclogae Geol. Helv. 87, 559–612.

Froitzheim, N., Plašienka, D., Schuster, R., 2008. Alpine tectonics of the Alps and Western Carpathians. In: McCann, T. (Ed.), The Geology of Central Europe. Geological Society of London 2, pp. 1141–1232 Mesozoic and Cenozoic.

Fügenschuh, B., Seward, D., Mancktelow, N.S., 1997. Exhumation in a convergent orogen: the western Tauern Window. Terra Nova 9, 213–217.

Genser, J., Neubauer, F., 1989. Low angle normal faults at the eastern margin of the Tauern Window (Eastern Alps). Mitt. Österr. Geol. Ges. 81, 233–243.

Genser, J., van Wees, J.D., Cloething, S., Neubauer, F., 1996. Eastern Alpine tectono-metamorphic evolution: constraints from two-dimensional P–T–t modeling. Tecton-ics 15, 584–604.

Grasemann, A., Mancktelow, N.S., 1993. Two-dimensional thermal modelling of normal faulting: the Simplon Fault Zone, Central Alps, Switzerland. Tectonophysics 225, 155–165.

Halama, R., Konrad-Schmolke, M., Sudo, M., Marschall, H., Wiedenbeck, M., 2014. Effects of fluid-rock interaction on $^{40}Ar/^{39}Ar$ geochronology in high-pressure rocks (Sesia-Lanzo Zone, Western Alps). Geochim. Cosmochim. Acta 126, 475–494. http://dx.doi.org/10.1016/j.gca.2013.10.023.

Hames, W.E., Bowring, S.A., 1994. An empirical evaluation of the argon diffusion geometry in muscovite. Earth Planet. Sci. Lett. 124 (1–4), 161–169.

Handy, M.R., Wissing, S., Streit, J.E., 1999. Strength and structure of mylonite with com-bined frictional-viscous rheology and varied bimineralic composition. Tectonophysics 303 (1–4), 175–192.

Handy, M.R., Schmid, S.M., Bousquet, R., Kissling, E., Bernoulli, D., 2010. Reconciling plate-tectonic reconstructions of Alpine Tethys with the geological–geophysical record of spreading and subduction in the Alps. Earth Sci. Rev. 102, 121–158. http://dx.doi.org/10.1016/j.earscirev.2010.06.002.

Harris, T.M., 1981. Diffusion of ^{40}Ar in hornblende. Contrib. Mineral. Petrol. 78, 324–331.

Harrison, M.T., Célérier, J., Aikman, A.B., Hermann, J., Heizler, M.T., 2009. Diffusion of ^{40}Ar in muscovite. Geochim. Cosmochim. Acta 73, 1039–1051.

Hawkesworth, C.J., 1976. Rb/Sr geochronology in the Eastern Alps. Contrib. Mineral. Petrol. 54, 225–244.

Inger, S., Cliff, R.A., 1994. Timing of metamorphism in the Tauern Window, Eastern Alps: Rb–Sr ages and fabric formation. J. Metamorph. Geol. 12, 695–707.

Ishizuka, O., 1998. Vertical and horizontal variations of the fast neutron flux in a single irradiation capsule and their significance in the laser-heating $^{40}Ar/^{39}Ar$ analysis: case study for the hydraulic rabbit facility of the JMTR reactor, Japan. Geochem. J. 32, 243–252.

Jäger, E., Niggli, E., Wenk, E., 1967. Rb–Sr Altersbestimmungen an Glimmern der Zentralalpen. Beitr. Geol. Karte Schweiz. 134, 67.

Kelley, S.P., Arnaud, N.O., Turner, S.P., 1994. High spatial resolution $^{40}Ar/^{39}Ar$ investiga-tions using an ultra-violet laser probe extraction technique. Geochim. Cosmochim. Acta 58, 3519–3525.

Ketcham, R.A., 1996. Thermal model of core-complex evolution in Arizona and New Guinea: implications for ancient cooling paths and present-day heat flow. Tectonics 15 (5), 933–951.

Kurz, W., Handler, R., Bertoldi, C., 2008. Tracing the exhumation of the Eclogite Zone (Tauern Window, Eastern Alps) by $^{40}Ar/^{39}Ar$ dating of white mica in eclogites. Swiss J. Geosci. 101 (1), 191–206.

Lammerer, B., Weger, M., 1998. Footwall uplift in an orogenic wedge: the Tauern Window in the Eastern Alps of Europe. Tectonophysics 285, 213–230.

Linzer, H.-G., Decker, K., Peresson, H., Dell'Mour, R., Frisch, W., 2002. Balancing lateral orogenic float of the Eastern Alps. Tectonophysics 354 (3/4), 211–237.

Lister, G.S., Snoke, A.W., 1984. S–C mylonites. J. Struct. Geol. 6 (6), 617–638.

Liu, Y., Genser, J., Handler, R., Friedl, G., Neubauer, F., 2001. $^{40}Ar/^{39}Ar$ muscovite ages from the Penninic–Austroalpine plate boundary, Eastern Alps. Tectonics 20, 526–547.

Luciani, V., Silvestrini, A., 1996. Planktonic foraminiferal biostratigraphy and paleoclima-tology of the Oligocene/Miocene transition from the Monte Brione Formation (Northern Italy, Lake Garda). Mem. Sci. Geol. 48, 155–170.

Ludwig, K.R., 2001. Isoplot/Ex version 2.49. A geochronological toolkit for Microsoft Excel. Berkeley Geochronology Center Special Publication No. 1a.

Ludwig, K.R., 2003. Isoplot/Ex version 3.0. A geochronological toolkit for Microsoft Excel. Berkeley Geochronological Centre Special Publication, Berkeley 70 p.

Luth, S.W., Willingshofer, E., 2008. Mapping of the post-collisional cooling history of the Eastern Alps. Swiss J. Geosci. 101 (1), 207–223.

Mulch, A., Cosca, M.A., Handy, M.R., 2002. In-situ UV-laser $^{40}Ar/^{39}Ar$ geochronology of a micaceous mylonite: an example of defect-enhanced argon loss. Contrib. Mineral. Petrol. 142, 738–752. http://dx.doi.org/10.1007/s00410-001-0325-6.

Neubauer, F., Genser, J., Kurz, W., Wang, X., 1999. Exhumation of the Tauern Window, Eastern Alps. Physics Chem. Earth (A) 24 (8), 675–680.

Peresson, H., Decker, K., 1997. The Tertiary dynamics of the northern Eastern Alps (Austria): changing palaeostresses in a collisional plate boundary. Tectonophysics 272, 125–157.

Pollington, A.D., Baxter, E.F., 2010. High resolution Sm–Nd garnet geochronology reveals the uneven pace of tectonometamorphic processes. Earth Planet. Sci. Lett. 293, 63–71.

Pomella, H., Klötzli, U., Scholger, R., Stipp, M., Fügenschuh, B., 2011. The Northern Giudicarie and the Meran-Mauls fault (Alps, Northern Italy) in the light of new paleo-magnetic and geochronological data from boudinaged Eo-/Oligocene tonalites. Int. J. Earth Sci. 100, 1827–1850. http://dx.doi.org/10.1007/s00531-010-0612-4.

Pomella, H., Stipp, M., Fügenschuh, B., 2012. Thermochronological record of thrusting and strike–slip faulting along the Giudicarie fault system (Alps, Northern Italy). Tectonophysics 579, 118–130. http://dx.doi.org/10.1016/j.tecto.2012.04.015.

Purdy, J.W., Jäger, E., 1976. K–Ar ages on rock-forming minerals from the Central Alps. Mem. Ist. Geol. Mineral. Univ. Padova 30.

Ratschbacher, L., Frisch, W., Linzer, H.-G., Merle, O., 1991. Lateral extrusion in the eastern Alps, part 2: structural analysis. Tectonics 10 (2), 257–271.

Reiners, P.W., Brandon, M.T., 2006. Using thermochronology to understand orogenic erosion. Ann. Rev. Earth Planet Sci. 34, 419–466.

Ring, U., Brandon, M., Willet, S., Lister, G., 1999. Exhumation processes. Geol. Soc. Lond. Spec. Publ. 154 (1), 1–27.

Rosenberg, C.L., Brun, J.P., Cagnard, F., Gapais, D., 2007. Oblique indentation in the Eastern Alps: insights from laboratory experiments. Tectonics 26, TC2003. http://dx.doi.org/10.1029/2006TC001960.

Royden, L.H., 1993. Evolution of retreating subduction boundaries formed during conti-nental collision. Tectonics 12 (3), 629–638.

Sander, B., 1911. Geologische Studien am Westende der hohen Tauern. Ber. Denkschrift kaiserlichen Akad. Wiss. Wien 83, 257–319.

Scharf, A., Handy, M.R., Favaro, S., Schmid, S.M., Bertrand, A., 2013a. Modes of orogen-parallel stretching and extensional exhumation in response to microplate indentation and slab roll-back (Tauern Window, Eastern Alps). Int. J. Earth Sci. 102 (6), 1627–1654. http://dx.doi.org/10.1007/s00531-013-0894-4.

Scharf, A., Handy, M.R., Ziemann, M.A., Schmid, S.M., 2013b. Peak-temperature patterns of polyphase metamorphism resulting from accretion, subduction and collision (eastern Tauern Window, European Alps) — a study with Raman microspectroscopy on carbonaceous material (RSCM). J. Metamorph. Geol. 31 (8), 863–880. http://dx.doi.org/10.1111/jmg.12048.

Schmid, S.M., Fügenschuh, B., Kissling, E., Schuster, R., 2004. Tectonic map and overall architecture of the Alpine orogen. Eclogae Geol. Helv. 97, 93–117.

Schmid, S.M., Bernoulli, D., Fügenschuh, B., Matenco, L., Schefer, S., Schuster, R., Tischler, M., Ustaszewski, K., 2008. The Alpine–Carpathian–Dinaridic orogenic system: correlation and evolution of tectonic units. Swiss J. Geosci. 101, 139–183.

Schmid, S.M., Scharf, A., Handy, M.R., Rosenberg, C.L., 2013. The Tauern Window (Eastern Alps, Austria) — a new tectonic map, cross-sections and tectonometamorphic synthesis. Swiss J. Geosci. 106, 1–32. http://dx.doi.org/10.1007/s00015-013-0123-y.

Schneider, S., Hammerschmidt, K., Rosenberg, C.L., 2013. Dating the longevity of ductile shear zones: insight from ^{40}Ar/^{39}Ar in situ analyses. Earth Planet. Sci. Lett. 369-370, 43–58. http://dx.doi.org/10.1016/j.epsl.2013.03.002.

Schuster, R., Frank, W., 2000. Metamorphic evolution of the Austroalpine units east of the Tauern Window: indications for Jurassic strike slip tectonics. Mitt. Ges. Geol. Bergbaustud. Österr. 42, 37–58.

Schuster, R., Koller, F., Hoeck, V., Hoinkes, G., Bousquet, R., 2004. Explanatory notes to the map: metamorphic structure of the Alps. Metamorphic evolution of the Eastern Alps. Mitt. Österr. Mineral. Ges. 149, 175–199.

Schuster, R., Pestal, G., Reitner, J.M., 2006. Erläuterungen zu Blatt 182 Spittal an der Drau. Geologische Karte der Republik Österreich 1:50.000. Geologische Bundesanstalt, Wien, p. 115.

Sciunnach, D., Scardia, G., Tremolada, F., Silva, I.P., 2010. The Monte Orfano Conglomerate revisited: stratigraphic constraints on Cenozoic tectonic uplift of the Southern Alps (Lombardy, northern Italy). Int J Earth Sci 99, 1335–1355. http://dx.doi.org/10.1007/ s00531-009-0452-2.

Selverstone, J., 1988. Evidence for east-west crustal extension in the Eastern Alps: implications for the unroofing history of the Tauern Window. Tectonics 7, 87–105.

Selverstone, J., Spear, F.S., Franz, G., Morteani, G., 1984. High-pressure metamorphism in the SW Tauern Window, Austria: P–T paths from hornblende–kyanite–staurolite schists. J. Petrol. 25, 501–531.

Seward, D., Vanderhaeghe, O., Siebenaller, L., Thomson, S., Hibsch, C., Zingg, A., Holzner, P., Ring, U., Duchêne, S., Wernicke, B., 2009. Cenozoic tectonic evolution of Naxos Island through a multi-faceted approach of fission-track analysis. In: Ring, U. (Ed.), Extending a Continent: Architecture, Rheology and Heat Budget. Geological Society, London, Special Publication 321, pp. 179–196. http://dx.doi.org/10.1144/SP321.9.

Simpson, C., Schmid, S.M., 1983. An evaluation of criteria to deduce the sense of movement in sheared rocks. Geol. Soc. Am. Bull. 94 (11), 1281–1288.

Sölva, H., Grasemann, B., Thöni, M., Thiede, R., Habler, G., 2005. The Schneeberg Normal Fault Zone: normal faulting associated with Cretaceous SE-directed extrusion in the Eastern Alps (Italy/Austria). Tectonophysics 401, 143–166.

Stampfli, G., Mosar, J., Favre, P., Pillevuit, A., Vannay, J.-C., 2001. Permo-Mesozoic evolution of the western Tethys realm: the Neo-Tethys East Mediterranean Basin connection. In: Ziegler, P.A., et al. (Eds.), Peri-Tethys Memoir 6: Peri-Tethyan Rift/Wrench Basins and Passive Margins. Mém. Muséum Natnional Hist. Nat. Paris 186, pp. 51–108.

Stipp, M., Stünitz, H., Heilbronner, R., Schmid, S.M., 2002. The eastern Tonale fault zone: a natural laboratory for crystal plastic deformation of quartz over a temperature range from 250 to 700 °C. J. Struct. Geol. 24, 1861–1884.

Stöckhert, B., Brix, M.R., Kleinschrodt, R., Hurford, A.J., Wirth, R., 1999. Thermochronometry and microstructures of quartz — a comparison with experimental flow laws and predictions on the temperature of the brittle–plastic transition. J. Struct. Geol. 21, 351–369.

ter Voorde, M., Bertotti, G., 1994. Thermal effects of normal faulting during rifted basin formation, 1. A finite difference model. Tectonophysics 240, 133–144.

Thöni, M., 1999. A review of geochronological data from the Eastern Alps. Schweiz. Mineral. Petrogr. Mitt. 79, 209–230.

Trümpy, R., 1960. Paleotectonic evolution of the Central and Western Alps. Geol. Soc. Am. Bull. 71, 843–908.

Uto, K., Ishizuka, O., Matsumoto, A., Kamioka, H., Togashi, S., 1997. Laser-heating ^{40}Ar/^{39}Ar dating system of the Geological Survey of Japan: system outlines and preliminary results. Bull. Geol. Surv. Jpn. 48, 23–48.

Villa, I.M., 2010. Disequilibrium textures vs equilibrium modelling: geochronology at the crossroads. In: Spalla, M.I., Marotta, A.M., Gosso, G. (Eds.), Advances in interpretation of geological processes. Geol. Soc. Lond., Spec. Publ. 332, pp. 1–15.

von Blanckenburg, F., Villa, I.M., 1988. Argon retentively and Argon Excess in Amphiboles from the Garbenschists of the Western Tauern Window, Eastern Alps. Contrib. Mineral. Petrol. 100, 1–11.

von Blanckenburg, F., Villa, I.M., Baur, H., Morteani, G., Steiger, R.H., 1989. Time calibration of a PT-path from the Western Tauern Window, Eastern Alps: the problem of closure temperatures. Contrib. Mineral. Petrol. 101, 1–11.

Wagner, G.A., Reimer, G.M., 1972. Fission track tectonics: the tectonic interpretation of fission track apatite ages. Earth Planet. Sci. Lett. 14 (2), 263–268.

Warren, C.J., Smye, A.J., Kelley, S.P., Sherlock, S.C., 2012. Using white mica ^{40}Ar/^{39}Ar data as a tracer for fluid flow and permeability under high-P conditions: Tauern Window, Eastern Alps. J. Metamorph. Geol. 30, 63–80. http://dx.doi.org/10.1111/j.1525-1314.2011.00956.x.

Wiederkehr, M., Sudo, M., Bousquet, R., Berger, A., Schmid, S.M., 2009. Alpine orogenic evolution from subduction to collisional thermal overprint: the ^{40}Ar/^{39}Ar age constraints from the Valaisan Ocean, Central Alps. Tectonics 28 (6), TC6009. http://dx.doi.org/10.1029/2009TC002496.